

Tellus B: Chemical and Physical Meteorology



ISSN: (Print) (Online) Journal homepage: https://www.tandfonline.com/loi/zelb20

A pragmatic protocol for characterising errors in atmospheric inversions of methane emissions over Europe

Barbara Szénási, Antoine Berchet, Grégoire Broquet, Arjo Segers, Hugo Denier van der Gon, Maarten Krol, Joanna J.S. Hullegie, Anja Kiesow, Dirk Günther, Ana Maria Roxana Petrescu, Marielle Saunois, Philippe Bousquet & Isabelle Pison

To cite this article: Barbara Szénási, Antoine Berchet, Grégoire Broquet, Arjo Segers, Hugo Denier van der Gon, Maarten Krol, Joanna J.S. Hullegie, Anja Kiesow, Dirk Günther, Ana Maria Roxana Petrescu, Marielle Saunois, Philippe Bousquet & Isabelle Pison (2021) A pragmatic protocol for characterising errors in atmospheric inversions of methane emissions over Europe, Tellus B: Chemical and Physical Meteorology, 73:1, 1-23, DOI: 10.1080/16000889.2021.1914989

To link to this article: https://doi.org/10.1080/16000889.2021.1914989



A pragmatic protocol for characterising errors in atmospheric inversions of methane emissions over Europe

By BARBARA SZÉNÁSI^{1*}, ANTOINE BERCHET¹, GRÉGOIRE BROQUET¹, ARJO SEGERS², HUGO DENIER VAN DER GON², MAARTEN KROL^{3,4}, JOANNA J.S. HULLEGIE², ANJA KIESOW⁵, DIRK GÜNTHER⁵, ANA MARIA ROXANA PETRESCU⁶, MARIELLE SAUNOIS¹, PHILIPPE BOUSQUET¹, and ISABELLE PISON¹, ¹Laboratoire des Sciences du Climat et de l'Environnement, LSCE-IPSL (CEA-CNRS-UVSQ), Université Paris-Saclay, Gif-sur-Yvette, France; ²TNO, Department of Climate, Air and Sustainability, Utrecht, The Netherlands; ³Wageningen University & Research, Wageningen, The Netherlands; ⁴Institute for Marine and Atmospheric Research Utrecht (IMAU), Utrecht University, The Netherlands; ⁵German Environment Agency, Unit Emission Situation, Dessau, Germany; ⁶Department of Earth and Life Sciences, Faculty of Science, Vrije Universiteit Amsterdam, Amsterdam, The Netherlands

(Manuscript Received 13 August 2020; in final form 7 April 2021)

ABSTRACT

This study aims at estimating errors to be accounted for in atmospheric inversions of methane (CH₄) emissions at the European scale. Four types of errors are estimated in the concentration space over the model domain and at selected measurement sites. Furthermore, errors in emission inventories are estimated at country and source sector scales. A technically ready method is used, which is implemented by running a set of simulations of hourly CH₄ mixing ratios for 2015 using two area-limited transport models at three horizontal resolutions with multiple data sets of emissions and boundary and initial conditions as inputs. The obtained error estimates provide insights into how these errors could be treated in an inverse modelling system for inverting CH₄ emissions over Europe. The main results show that sources of transport errors may better be controlled alongside the emissions, which differs from usual inversion practices. The average total concentration error is estimated at 29 ppb. The assessed error of total CH₄ emissions is 22% and emission errors are heterogeneous at sector (23–49%) and country scales (16–124%), with largest errors occurring in the waste sector due to uncertainties in activity data and emission factors and in Finland due to uncertainties in natural wetland emissions.

Keywords: methane, Europe, error estimation, atmospheric inversion

1. Introduction

Methane (CH₄) contributed up to 11% to the total greenhouse gas (GHG) emissions of the European Union (EU) in 2017 (EEA, 2019), after carbon dioxide (79%). In Europe, CH₄ is released to the atmosphere by a variety of anthropogenic (more than 80%) and natural (\sim 20%) sources (Saunois et al., 2016a, 2016b). Anthropogenic CH₄ mainly originates from the activity of anaerobic bacteria in waste water treatment, landfills and agriculture,

mainly through manure management and enteric fermentation of ruminants. Anthropogenic CH₄ is also released during fossil fuel extraction, production and distribution, non-industrial combustion (e.g. heating), the use of biofuel, as well as through rice cultivation, biomass burning from agricultural activities and the treatment of agricultural waste. The largest anthropogenic emission sources in the EU are enteric fermentation, manure management and anaerobic waste treatment, accounting for \sim 54% of the total anthropogenic sources in 2017 (EEA, 2019). Natural sources include methanogenesis in natural

^{*}Corresponding author. e-mail: barbara.szenasi@lsce.ipsl.fr

wetlands mostly, and to a lesser extent CH₄ release in natural gas seeps and by wildfires, through incomplete combustion of the biomass.

Due to CH₄'s relatively short atmospheric lifetime of 8-10 years (IPCC, 2013), it is a good target for shortterm climate change mitigation. In order to design efficient mitigation strategies, it is necessary to have an advanced understanding on the magnitudes, trends, as well as spatial, temporal and sector distributions of CH₄ emissions at the relevant space and time scales. Emissions are defined by activity data and emission factors. The first term refers to anthropogenic socio-economic activities causing emissions, while the second term quantifies sources or sinks per unit of activity (IPCC, 2006). Emissions are primarily estimated and characterised by the so-called bottom-up approaches; (i) aggregating socio-economic statistical information in the case of anthropogenic emission inventories (e.g. Kuenen et al., 2014), (ii) using process-based numerical models calibrated with local-scale measurements and lab experiments (e.g. Ringeval et al., 2010) or (iii) upscaling local models and measurements (e.g. Peltola et al., 2019). However, the large variety of anthropogenic sources associated with high heterogeneity, both in space and time, of their activity data and emission factors leads to imperfect knowledge. All emission data sets have significant but illquantified uncertainties, of which the statistical characterisation is particularly difficult (Jonas et al., 2011).

An alternative to bottom-up approaches is proposed by top-down atmospheric inversions. The aim of such an approach is to reduce uncertainties on existing emission data sets. They are built to optimally merge atmospheric measurements, numerical modelling of atmospheric transport and chemistry and prior knowledge on emissions. Atmospheric inversions commonly apply Bayesian inversion methods (Tarantola, 2005) using bottom-up emission data sets as prior knowledge and assimilating atmospheric mixing ratio data in a chemistry-transport model (CTM) to update this prior knowledge into an optimised posterior emission estimate. In principle, the Bayesian framework makes it possible to obtain the information about the emissions contained in the misfits between the model simulations and the measurements from the other sources of errors, assuming that the statistics of the different types of errors are correctly characterised. Misfits between model simulations and measurements originate from (i) errors in measurements (instrument precision and accuracy), (ii) uncertainties in the chosen prior emission inventory, (iii) projection of emissions to the CTM's grid, (iv) representativity of simulated mixing ratios in a model grid cell compared to measurements, which can generally be viewed as representative of a point (for in situ measurements) or a line (for remote-sensing data), compared to the typical spatial and temporal resolution of CTMs, (v) boundary conditions used in the CTM for the case of regional CTMs with limited-area domains of simulation, (vi) uncertainties in the modelling of the transport in the CTM itself (discretisation and numerical solving of continuous equations, physical parameterisations and simplifications, uncertainties in the meteorological forcing), as well as (vii) aggregation errors, which are due to the spatial and temporal resolutions of the inversion, which are different from (usually coarser than) the spatial and temporal resolutions of the CTM.

To date, atmospheric studies for the inversion of CH₄ emissions use configurations which have been specifically adapted to each inversion system and inverse problem to be solved (e.g. Bergamaschi et al., 2005, 2018; Thompson et al., 2015; Henne et al., 2016; Tsuruta et al., 2019; Wang et al., 2019.) In particular, uncertainties in inverse systems are based on approximations, past experience and expert knowledge, which can be biased towards including some specific error-generating processes and ignoring others, for example, taking into account errors due to the vertical mixing in the model and not the errors due to the representation of sub-grid-scale processes. Recent studies have proposed automatic methods representing uncertainties in inversion systems in a more comprehensive way (e.g. Ganesan et al., 2014; Berchet et al., 2015; Lunt et al., 2016; Pison et al., 2018; McNorton et al., 2020). These studies are based on Monte Carlo approach, systematic exploration of possible uncertainties and/or objective analysis of available data to estimate uncertainties. They primarily optimise the uncertainties in all sources of model-data misfits along with the posterior emissions and uncertainties. Still, underlying assumptions are strong (such as structure of errors and their correlation) and methods are computationally very expensive, making their application hard to replicate, especially for high dimensional problems with emissions at high spatial and temporal resolutions and with large amounts of observations to assimilate.

The replicability and operationality of the uncertainty assessment is especially critical in the field of regional atmospheric inversions of CH₄ emissions, with high pressure to deliver reliable results to policy makers in the framework of the Paris Agreement. As the volume of observations will further increase (Bousquet et al., 2018; Hu et al., 2018; Varon et al., 2019), our capability of manually attributing uncertainties will be more and more compromised. Indeed, in the EU, the increasing availability of continuous *in situ* observations (mainly in the ICOS network, https://www.icos-cp.eu/), of ground-based remote-sensing data (for example, total columns in Wunch et al., 2019) and of high-resolution satellite

products, makes it necessary to build generic and efficient tools to consistently quantify uncertainties.

In this study, our aim is to obtain uncertainty estimates, which can be used in the framework of inversions of CH₄ emissions in Europe by assimilating in situ measurements from surface stations. To obtain these uncertainty estimates, we use a methodology that is computationally inexpensive, easy to reproduce and to update. Easy updating makes it possible to compute improved estimates by including new data products (e.g. new prior emission inventories, meteorology products at high resolutions), covering extended measurement periods, taking into account new measurement sites or largesize data sets (e.g. satellite data). The uncertainty estimates obtained here should help setting-up inversions by providing insights on (i) how to account for sources of errors that are not emission related (e.g. transport with the CTM parameterizations and discretization) and (ii) how to specify error statistics (magnitude, temporal and spatial patterns of errors). The uncertainty estimates are computed at the CTM's grid resolution and at hourly scales, which are the finest targeted resolution for the foreseen inversions. The spatial and temporal scales targeted by the inversion can also be coarser than the CTM's: in Europe, a primary target for CH₄ could be estimates of emissions at country scale per sector per year or per month.

Following Wang et al. (2017), we base our error analysis and practical implementation on comparisons between simulation outputs and in situ measurements of CH₄ mixing ratios, as generated from an ensemble of model simulations. The ensemble of simulations covers the year 2015 and is based on available tools: three inventories of European anthropogenic CH₄ emissions, three data sets of natural wetland CH₄ emissions, two CTMs with three different horizontal resolutions and two sets of lateral boundary conditions (LBCs). The data sets and the models are described in Section 2. The methodology to compute error estimates is explained in Section 3, where we analyse the magnitude of errors and investigate to what extend they are correlated in time and space. The results are presented and discussed in Section 4, with emphasis on the relations between the different errors. Finally, Section 5 concludes about possible error characterisations and ranges and ways to use these results in atmospheric inversions of European CH₄ emissions.

2. Data and model description

2.1. Measurements

In this study, focussed on the year 2015, we use hourly atmospheric measurements of CH₄ mixing ratios for at

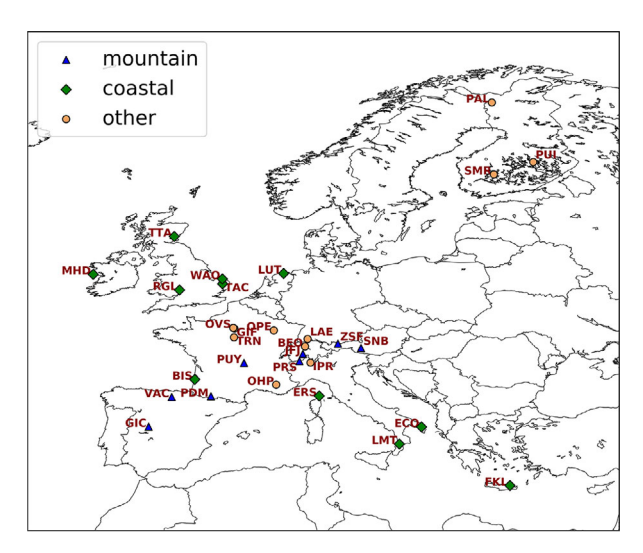


Fig. 1. Locations of the 31 selected measurement sites (with at least six months of data available for 2015, see details in Table S1). Blue triangles indicate mountain sites, green diamonds coastal sites and orange circles indicate 'other' sites that are not included in the first two categories.

least six months in the year. We originally choose 2015 for the analysis as a large number of measurements are available for this year, used to compare simulation outputs to measurements for choosing the appropriate model layer (see Section 3.2). The selected 31 measurement sites in Europe are listed in Table S1 and their locations are shown in Fig. 1.

In order to identify links between error statistics and locations and surrounding topography of the measurement sites, we group the measurement sites in three categories: mountain sites, coastal sites and other sites (in most cases, tall towers at rural sites in a relatively flat environment). When a measurement site provides several sampling heights, we use the highest level to limit the effects of local emissions. That, combined with poorly resolved vertical transport near the surface, may lead to biased inversions (Broquet et al., 2011).

2.2. Emissions

Three annual anthropogenic gridded emission inventories are used: the TNO-MACC_III (Kuenen et al., 2014), the EDGAR v4.3.2 (Janssens-Maenhout et al., 2019) and the ECLIPSE V5a (Stohl et al., 2015). At the start of this study, the inventories did not include the year 2015 so that we use the emissions from the most recent year available in each inventory (Table S2).

For this study, CH₄ emissions are grouped into Selected Nomenclature for Air Pollution (SNAP) level-1 sectors to have a common ground for the three inventories, as they use different classifications. In our European

Table 1. Total and sectoral emissions [Tg CH₄ year⁻¹] of the TNO-MACC_III, EDGAR v4.3.2 and ECLIPSE V5a anthropogenic inventories in our European domain.

		Emissions (Tg CH ₄ year ⁻¹)			% of total anthropogenic emissions		
SNAP code	Details	TNO-MACC_III (2011)	EDGAR v4.3.2 (2011)	ECLIPSE V5a (2010)	TNO-MACC_III	EDGAR v4.3.2	ECLIPSE V5a
2&5	Non-industrial combustion plants & Distribution of fossil fuels and geothermal energy	6.1	7.3	5.9	24.0	23.9	22.6
9	Waste treatment and disposal	7.7	10.8	7.8	30.3	35.3	29.9
10	Agriculture	10.9	12.1	12.0	42.9	39.5	45.8
All	Total anthropogenic	25.4	30.6	26.1	97.2	98.7	98.5

The three main sectors used in this study are described in column 'Details'.

domain, agriculture (SNAP 10) is the main emitting sector, followed by the waste sector (SNAP 9). Other relevant emission sources for CH₄ are non-industrial combustion plants (SNAP 2) and the production, extraction and distribution of fossil fuels (SNAP 5). The latter two were added into one category that is named 'fossil fuel related emissions' hereafter (Table 1). The total anthropogenic emissions in EDGAR v4.3.2 are up to 20% larger than in TNO-MACC_III and ECLIPSE V5a but the relative contributions of the three main sectors are very similar across the inventories (Table 1). The agriculture sector dominates (about 39-46% of the total CH₄ emissions). In this sector, emissions in EDGAR v4.3.2 and TNO-MACC_III are large over Brittany in France, the BENELUX and some Eastern European countries (e.g. Romania, Belarus), while emissions in ECLIPSE V5a are larger than those of EDGAR v4.3.2 and TNO-MACC_III over the Po Valley and generally in Italy. For the waste sector, ECLIPSE V5a generally attributes larger emissions in most countries, while EDGAR v4.3.2 and TNO-MACC_III are large in some individual grid cells. For the fossil fuel related emissions, the largest differences between the three inventories exist over the North Sea and the Ukraine, where the emissions in ECLIPSE V5a are larger than those of the other two inventories.

Furthermore, we use three data sets of natural CH_4 emissions to characterise errors from wetland emissions: ORCHIDEE-WET (Ringeval et al., 2011), CLASS-CTEM (Arora et al., 2018) and JULES (Hayman et al., 2014). Even though these process models provide wetland CH_4 emissions on a monthly time scale, we use yearly emissions to stay consistent with the choice of

anthropogenic emissions (Table S3). The sum of ORCHIDEE-WET emissions (7.8 Tg CH₄ year⁻¹) over the domain is more than twice as high as that of CLASS-CTEM (3.7 Tg CH₄ year⁻¹) and JULES (3.2 Tg CH₄ year⁻¹). The top panel of Fig. 2 shows the averaged spatial distribution of the total and sectoral emissions for both anthropogenic and natural sources.

2.3. Chemistry-transport models

We use two regional CTMs: CHIMERE (Menut et al., 2013; Mailler et al., 2017) driven by the system PYVAR (Fortems-Cheiney et al., 2019) and LOTOS-EUROS (Manders et al., 2017) in a European domain covering $[31.5^{\circ}-74^{\circ}]$ in latitude and $[-15^{\circ}-35^{\circ}]$ in longitude (Fig. 1). The main characteristics of the set-up of the two models can be found in Table 2. The meteorological data used to drive both models are obtained from the European Centre for Medium-Range Weather Forecast (ECMWF) operational forecast product. For the CHIMERE simulations, the boundary and initial concentrations of CH₄ are taken either from the analysis and forecasting system developed in the Monitoring Atmospheric Composition and Climate (MACC) project (Marécal et al., 2015) or are pre-optimized LBCs. The pre-optimized LBCs are 4D fields of CH₄ concentrations resulting from the inversion by Bousquet et al. (2006), using the global scale Laboratoire de Météorologie Dynamique (LMDz) model (Hourdin et al., 2006). The most recent available year from this inversion system is 2010, which we use to provide large-scale patterns and seasonal cycles at the boundaries of our domain for 2015.

Model	CHIMERE	LOTOS-EUROS
Meteorology	ECMWF	ECMWF
Horizontal resolution	$10\times10\mathrm{km}$	$7 \times 7 \text{ km}$
Frequency of data availability	3 h	3 h
Boundary and initial conditions	LMDz or MACC	CH ₄ : CAMS CH ₄ flux reanalysis, full
Vertical levels	19 & 71	chemistry runs: MACC
Horizontal resolution (lon \times lat)	$3.75^{\circ} \times 2.5^{\circ} \& 0.653^{\circ} \times 0.653^{\circ}$	34
Frequency of data availability	48 h & 3 h	$3^{\circ} imes 2^{\circ}$
		3 h
Number of levels	29	20
Top pressure	300 hPa	240 hPa
Anthropogenic emissions	EDGAR v4.3.2 or TNO-MACC_III	EDGAR v4.3.2 or TNO-MACC_III
	or ECLIPSE V5a	or ECLIPSE V5a
Horizontal resolutions (lon \times lat)	$0.5^{\circ} \times 0.5^{\circ}$ or $0.25^{\circ} \times 0.25^{\circ}$ or $0.5^{\circ} \times 0.25^{\circ}$	$0.5^{\circ} imes 0.25^{\circ}$
Period simulated	2015	2015

Table 2. Set-ups and input data for the atmospheric chemistry–transport models CHIMERE and LOTOS-EUROS for the simulations in 2015.

The resolutions indicated for Meteorology and Boundary and initial conditions are the original ones, from which the data is interpolated on the Horizontal resolutions.

The CH₄ boundary and initial conditions of the LOTOS-EUROS model are taken from the CAMS CH₄ reanalysis product (Segers and Houweling, 2017). The global concentration fields and meteorological products were interpolated to our models' resolutions both spatially and temporally.

3. Methodology

3.1. Definition of error sources

We study five errors, described below; one of them is in the emission space and four are in the concentration space:

Error in the emission space:

 e_p , called hereafter the prior error, which is the error of the emissions in the inventories and process models, particularly due to the spatial distribution of the emissions at the sector and country scales. This error source includes the errors due to the projection of the inventories on the model's grid and due to the use of different methodology, socio-economic input data and products used for the spatial distribution of emissions in various inventories. The inventories use the E-PRTR database (http://prtr.ec.europa.eu/) for the location of facilities but when no information is found on specific sources, internal databases or other proxies, such as rural or urban population, are used. For example, for the spatial distribution of landfills, EDGAR v4.3.2 uses the E-PRTR database, while TNO-MACC_III makes use of E-PRTR and rural population density. The temporal distribution of e_p is not studied as emissions do not vary throughout the year in the inventories used here. In terms of statistics, larger numbers (>three) of inventory-based emission maps would be required to compute a more robust estimate of $e_{\rm p}$. However, in practice, we do not have access to an ensemble of perturbed emission maps from inventory models for gridded ${\rm CH_4}$ emission inventories covering Europe.

Errors in the concentration space:

- $\epsilon_{\rm flx}$ called hereafter the transported-emission error. This error source is due to the impact of the errors in the emission inventories on the simulated mixing ratios in the transport model domain. The error $e_{\rm p}$ is linked to $\epsilon_{\rm flx}$ mainly through the projection of the inventories on the model's grid and the atmospheric transport of these emissions by the model;
- ε_{repr} the representation error, due to the model having a resolution that is coarser than the scales at which emissions vary and of which *in situ* measurements are representative;
- ε_t the transport error, due to discretisation with subgrid scale parametrisations and other approximations of the fundamental equations of the atmospheric transport used in a model. Further causes of ε_t are the meteorological forcing (computed off-line for the CTMs used here, by the numerical weather forecast system of ECMWF) and the choice of physical approximations used in a given model. The part of the transport uncertainties arising from the meteorological forcing is limited by the use of ECMWF products used for the two CTM configurations. However, these two CTMs are driven by two different versions of the ECMWF forecast product (see

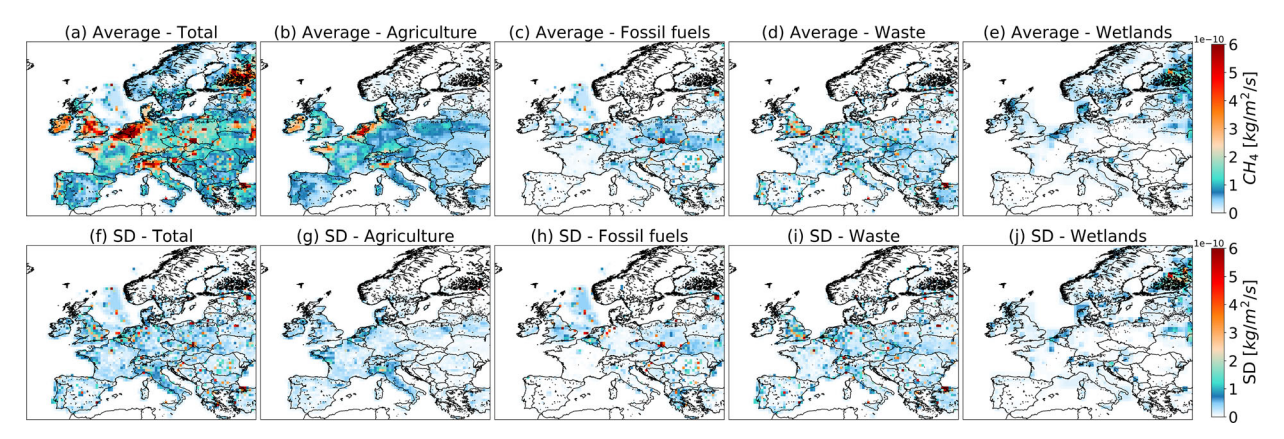


Fig. 2. Average (top, in kg m⁻² s⁻¹) and standard deviations (SDs, bottom, in kg m⁻² s⁻¹) of yearly CH₄ emissions from the anthropogenic and natural data sets: total, three main anthropogenic emission sectors and natural wetland emissions (see Section 2.2 for definition).

Table 2). We thus provide an estimate of the transport error including uncertainties in the meteorological forcing, even though this component might be underestimated.

• ϵ_{LBC} , called hereafter the background error, is due to the choice of lateral boundary conditions (LBCs, four sides and top of the domain) and initial conditions.

As the air masses in the analysed limited-area domain change in approximately 10-14 days and this study focuses on errors near the surface during only one year, which is shorter than the atmospheric lifetime of CH₄, errors due to the representation of atmospheric sink processes in the two CTMs are not considered here. Furthermore, this list of errors does not include the aggregation error described in Wang et al. (2017), which is based on Kaminski et al. (2001) and Bocquet et al. (2011). This error is linked to the inversion targeting emissions at a resolution coarser than the CTM's resolution. To our knowledge, inversion systems do not use the CTM's native spatio-temporal resolution as a target resolution. In many cases, the CTM's grid cells are grouped into coarser spatial structures (e.g. national or regional groups) and in most cases, the temporal profiles of emissions are grouped by time periods (from a few hours to days or even years), below which a constant profile is kept throughout the inversion procedure. Inversions with the capability to handle large control vectors, like variational inversions, often control the emissions at a resolution close to that of the transport model (e.g. Broquet et al., 2011; Fortems-Cheiney et al., 2012), at least spatially. In that case, ε_{flx} covers most of the aggregation error. In contrast, for inversions handling low resolution control vectors (e.g. Pison et al., 2018), like when using analytical inversion systems, the aggregation error can dominate over many other type of errors (Wang et al., 2017). Here, considering our future use of a variational inverse modelling system in which all spatial and temporal scales can be targeted (from the grid-cell and hourly scales to the whole domain and period of interest), we do not further investigate the aggregation error. Our aim is to estimate the dominant contributions to the total transport model and prior errors in order to propose a lower bound for uncertainties and consistent structures of errors.

To evaluate whether an atmospheric inversion is relevant to tackle the targeted CH₄ emissions, we compare the magnitudes and structures of ϵ_{repr} , ϵ_t and ϵ_{LBC} to ϵ_{flx} . The relation of ϵ_{flx} to the other errors in the concentration space is valuable as ϵ_{flx} contains the expected signal from emissions in the simulated mixing ratios. Several cases are possible:

- efix has distinct spatio-temporal structures and/or dominates all other types of error: emissions are so ill-quantified, that is, ep is large and is not smoothed out when projected by the model to the concentration space (through mainly the projection of the inventory on the model's grid and the simulation of the atmospheric transport), that they introduce large errors on the simulated mixing ratios. Therefore, any data brings valuable knowledge on emissions in an inversion. This can be the case of particular sectors with little or no reliable information on emissions;
- errors have similar structures and some errors are of the same magnitude as ϵ_{flx} : the inversion may lead to inconclusive ambiguous results;
- errors have similar structures and some errors are large compared to ϵ_{flx} : the inversion is likely to bring only limited information and only on very large scale aggregated CH_4 budgets; in that case, it

may be possible to control the sources of these errors alongside the CH₄ emissions to better optimise the latter; for instance, regional inversions classically include LBCs in their control vector to avoid biases in the LBCs impacting emission estimates. In Section 4.2.2, we elaborate on this issue.

3.2. Estimates of the representation error ϵ_{repr} , the transport error ϵ_{t} , the transported-emission error ϵ_{flx} and the background error ϵ_{LBC} from simulated CH_4 mixing ratios

Following Wang et al. (2017), from the available modelling components (Table 2), a total of 11 CHIMERE and three LOTOS-EUROS simulations are run as listed in Table 3. In each grid cell c, one estimate of a given ϵ_i , for $i \in \{\text{repr}, t, flx, LBC\}$, consists of a time-series of hourly differences between two simulations, ϕ and ψ , of CH₄ concentrations which differ by only one aspect:

$$\varepsilon_{i,c}^{(\phi,\psi)} = ([CH_4]_{c,h}^{\phi} - [CH_4]_{c,h}^{\psi})_{h \in H}$$
 (1)

with H an ensemble of hours among all the 8760 h in 2015.

The 14 simulations available are grouped to compute:

• Three estimates of $\varepsilon_{\rm repr}$: (R1ED-R2ED), (R1TM-R2TM), (R1EC-R2EC); each calculation is based on two horizontal resolutions, $0.5^{\circ} \times 0.5^{\circ}$ and $0.25^{\circ} \times 0.25^{\circ}$, and one inventory per estimate. The differences are computed in the grid cells of the finer resolution after merging the coarser resolution on the fine resolution grid (one grid cell at $0.5^{\circ} \times 0.5^{\circ}$ corresponds to four grid cells at $0.25^{\circ} \times 0.25^{\circ}$). This can

lead to additional errors, which however, are assumed to be small compared to the differences between the simulation outputs made with different horizontal resolution configurations. This estimation method takes only the horizontal representation error into account. Accounting for both the vertical and horizontal components of the representation error would yield a more comprehensive estimate of $\epsilon_{\rm repr}$. However, the way we sample the simulation outputs (see last paragraph of this section) should limit the vertical component of the representation error.

- Three estimates of ε_t: (T1ED-T2ED), (T1TM-T2TM), (T1EC-T2EC); each calculation is based on the two CTMs computed at the same horizontal resolution (0.5° × 0.25°) and one inventory per estimate. This gives insights into transport error characteristics as different CTMs apply different parameterisations, physical approximations, etc. Nevertheless, in terms of statistics, it should be noted that a larger ensemble of different CTMs would allow a better quantification of ε_t.
- Three estimates of ε_{flx}: (IED-ITM), (ITM-IEC), (IEC- IED); each calculation is based on a pair of the three anthropogenic inventories computed with the model CHIMERE at 0.5° × 0.5°.
- One estimate of ε_{LBC}: (L1-L2), based on the two available LBC data set runs with CHIMERE at 0.5° × 0.5°. Similarly to ε_t, ε_{LBC} could be better quantified with more than two LBC data sets. However, at the time of the study, only a limited number of CH₄ LBC data sets were available.

Table 3.	Simulations	performed	with th	ne set-ups	of the tw	chemistry	–transport m	odels (CTMs)	described in Tabl	le 2.
----------	-------------	-----------	---------	------------	-----------	-----------	--------------	--------------	-------------------	-------

CTM	Boundary conditions	Emissions	Resolution (lon \times lat)	ID
CHIMERE	MACC	EDGAR v4.3.2	$0.5^{\circ} \times 0.5^{\circ}$	R1ED, IED
CHIMERE	MACC	EDGAR v4.3.2	$0.25^{\circ} \times 0.25^{\circ}$	R2ED
CHIMERE	MACC	EDGAR v4.3.2	$0.5^{\circ} \times 0.25^{\circ}$	T1ED
CHIMERE	MACC	TNO-MACC_III	$0.5^{\circ} imes 0.5^{\circ}$	R1TM, ITM
CHIMERE	MACC	TNO-MACC_III	$0.25^{\circ} \times 0.25^{\circ}$	R2TM
CHIMERE	MACC	TNO-MACC_III	$0.5^{\circ} \times 0.25^{\circ}$	T1TM
CHIMERE	MACC	ECLIPSE V5a	$0.5^{\circ} imes 0.5^{\circ}$	R1EC, IEC
CHIMERE	MACC	ECLIPSE V5a	$0.25^{\circ} \times 0.25^{\circ}$	R2EC
CHIMERE	MACC	ECLIPSE V5a	$0.5^{\circ} \times 0.25^{\circ}$	TEC
CHIMERE	MACC	EDGAR v4.3.2	$0.5^{\circ} \times 0.5^{\circ}$	L1
CHIMERE	LMDZ	EDGAR v4.3.2	$0.5^{\circ} \times 0.5^{\circ}$	L2
LOTOS-EUROS	CAMS	EDGAR v4.3.2	$0.25^{\circ} \times 0.25^{\circ}$	T2ED
LOTOS-EUROS	CAMS	TNO-MACC_III	$0.5^{\circ} \times 0.25^{\circ}$	T2TM
LOTOS-EUROS	CAMS	ECLIPSE V5a	$0.5^{\circ} \times 0.25^{\circ}$	T2EC

The ID(s) attributed to each simulation indicate(s) when it is used for computing differences between different resolutions (R1X-R2X, with X = ED, TM or EC, i.e. one of the inventories), between different inventories (IX_1-IX_2), between different transport models (T1X-T2X) or between different boundary conditions (L1-L2). See Section 3.2 for details.

As this study is a first step towards regional inversion using real in situ observations, all estimates of errors are also calculated in the grid cells matching the horizontal and vertical location of existing measurements in Europe (see Table S1). To determine the model layer that best fits the height of the measurements for each site, the root mean square error (RMSE) between measured and simulated hourly mixing ratios from 2015 was computed for all the model layers; the layer with the lowest RMSE was then taken to compute error estimates. As CHIMERE uses hybrid σ pressure coordinates that feature small variations of a few metres over time, seasonal effects on the model layer selection are likely negligible. Note that choosing another layer than the one with the lowest RMSE would lead to an increase of the errors in the concentration space.

3.3. Metrics characterising errors

To be able to summarise estimates of error time-series, we define aggregated metrics used later in Section 4. The chosen metrics are the bias (even though bias can be negative or positive, here we are interested only in the magnitude of it), the standard deviation of errors, the spatial correlation of errors as well as the temporal correlation of errors on a given sub-sample H of hours in 2015 (see details on the choice of H in Section 3.4).

For every estimate (ϕ,ψ) of a given error $i\in\{\text{repr},\mathsf{t},\text{flx},\text{LBC}\}$, we compute the bias $b_{\varepsilon_{i,e,H}^{(\phi,\psi)}}$ and the standard deviation $\sigma_{\varepsilon_{i,e,H}^{(\phi,\psi)}}$ as:

$$\begin{cases} b_{\varepsilon_{i,c,H}^{(\phi,\psi)}} &= \overline{\varepsilon_{i,c}^{(\phi,\psi)}} = \frac{1}{Card(H)} \sum_{h \in H} \varepsilon_{i,c,h}^{(\phi,\psi)} \\ \sigma_{\varepsilon_{i,c,H}^{(\phi,\psi)}} &= \sqrt{\frac{1}{Card(H)}} \sum_{h \in H} (\varepsilon_{i,c,h}^{(\phi,\psi)} - b_{\varepsilon_{i,c,H}^{(\phi,\psi)}})^2 \end{cases}$$
 (2)

with Card(H) being the size of the sample H.

The spatial correlations of an estimate (ϕ, ψ) of a given error $i \in \{\text{repr}, t, \text{flx}, \text{LBC}\}$ are obtained from the biascorrected correlations for pairs of grid cells (c_1, c_2) :

$$corr_{i,(c_{1},c_{2}),H}^{(\phi,\psi)} = \frac{\frac{1}{Card(H)} \sum_{h \in H} \left(\varepsilon_{i,c_{1},h}^{(\phi,\psi)} - b_{\varepsilon_{i,c_{1},H}^{(\phi,\psi)}} \right) \left(\varepsilon_{i,c_{2},h}^{(\phi,\psi)} - b_{\varepsilon_{i,c_{2},H}^{(\phi,\psi)}} \right)}{\sigma_{\varepsilon_{i,c_{1},H}^{(\phi,\psi)}} \times \sigma_{\varepsilon_{i,c_{2},H}^{(\phi,\psi)}}}$$

$$(3)$$

The correlations are represented as the average of all correlations from all possible pairs for a given distance interval (Section 4.2.4):

$$corr_{i,d,H}^{(\phi,\psi)} = \overline{\left\{corr_{i,(c_1,c_2),H}^{(\phi,\psi)} \ \forall (c_1,c_2) \setminus ||c_1c_2|| \in [d,d+50 \text{km}]\right\}}$$

$$\tag{4}$$

The temporal auto-correlation R for a given temporal delay k (with unit days) is computed as follows:

$$R_{i,c,H}^{(\phi,\psi)}(k) = \frac{\frac{1}{Card(H)} \sum_{h \in H} \left(\varepsilon_{i,c,h}^{(\phi,\psi)} - b_{\varepsilon_{i,c,H}^{(\phi,\psi)}} \right) \left(\varepsilon_{i,c,h+k}^{(\phi,\psi)} - b_{\varepsilon_{i,c,H}^{(\phi,\psi)}} \right)}{\sigma_{\varepsilon_{i,c,H}^{(\phi,\psi)}}}$$
(5)

In most inversion studies, the temporal correlation of errors is assumed to follow an exponential decay. In our case, the auto-correlations quickly decrease before converging to zero but do not necessarily closely follow an exponential decay. Nevertheless, for a simple representation of the temporal correlation, we take the time after which the auto-correlation drops below e^{-1} .

For better readability, the spatial distribution of the metric of a given error $i \in \{\text{repr}, t, \text{flx}, \text{LBC}\}$ is not displayed for all possible estimates (e.g. for all pairs of inventories). Instead, we show the average of the metric of interest on all estimates of the error (one for ϵ_{LBC} , and three for all other errors, as detailed in Section 3.2) in Sections 3.4, 4.2.1–4.2.3.

3.4. Temporal sampling of error time series

To investigate whether a diurnal cycle is present in the error metrics, we compute the estimates of $\varepsilon_{\text{repr}}$, ε_{t} , ε_{flx} , ε_{LBC} for eight sub-samples W_j of simulated hourly concentrations over 3-h long time-windows j:

$$W_i = [(3j)\text{hours}; (3j+3)\text{hours}] \tag{6}$$

To detect whether there is a period in the day which is more favourable for assimilating observations on regional scale, we compute the ratios of the averages of $\varepsilon_{\text{repr}}$, ε_{t} and ε_{LBC} with respect to ε_{flx} , for each time-window j, in each grid cell c:

$$r_{i,c}^{j} = \frac{\overline{\varepsilon_{i,c}^{j}}}{\varepsilon_{g_{N,c}}^{j}} \text{ with } i \in \{\text{repr}, t, LBC}\}$$
 (7)

We subsequently determine the minimum and maximum of $r_{i,c}^{j}$ for each $i \in \{\text{repr}, t, \text{LBC}\}$ to signal the time-window for which the ratio of errors to ϵ_{flx} is the smallest. These values are shown and the results described for the locations c of the measurement sites in Fig. S1 in Section S3 of the Supplementary material. The results differ from the choice generally made in inversions, based on expert knowledge, to select only afternoon observations for non-mountain sites to limit the impact of poorly-modelled shallow planetary boundary layer (PBL) during the night and early morning. Indeed, the vertical

mixing and its impact on the diurnal cycle of mixing ratios are a significant source of error in CTMs (Dabberdt et al., 2004; Locatelli et al., 2015; Koffi et al., 2016). However, both CTMs in this study use ECMWF data so that errors on the vertical mixing likely follow the same diurnal pattern. It is therefore not possible here to go further in the analysis of the impact of the errors on the vertical mixing at the sub-diurnal scale. In order to stay compatible with the usual choice of afternoon observations for non-mountain sites, in the following, we compute ε_{repr} , ε_t , ε_{flx} , ε_{LBC} in each grid cell c from simulated hourly concentrations between 13h and 17h UTC included. For mountain sites, we take the simulated hourly concentrations between 00 h and 04 h UTC included. The sample of hourly concentrations H to compute error metrics has then $5 \text{ h} \times 365 \text{ days} = 1825 \text{ ele-}$ ments. Our computation of the transport error thus focuses on the horizontal aspect, rather than the vertical one.

3.5. Indicators of e_p characteristics

As the horizontal resolutions of the emission inventories differ, the emissions are spatially interpolated onto the model grids with conserving at least 99% of the mass. The consistency of the spatial distributions of the inventories is represented through the average and standard deviation (SD) of CH_4 emissions per sector s in each grid cell c (Fig. 2):

$$\overline{f_{s,c}} = \frac{1}{3} \left(f_{s,c}^{ED} + f_{s,c}^{TM} + f_{s,c}^{EC} \right)$$
 (8)

$$SD_{s,c} = \frac{\sqrt{\frac{1}{3}\left((f_{s,c}^{ED} - \overline{f_{s,c}})^2 + (f_{s,c}^{TM} - \overline{f_{s,c}})^2 + (f_{s,c}^{EC} - \overline{f_{s,c}})^2\right)}}{\overline{f^{s,c}}} \times 100$$
(9)

with f^{XY} the annual emissions from EDGAR v4.3.2 (XY = ED), TNO-MACC_III (XY = TM) and ECLIPSE V5a (XY = EC).

To investigate whether the prior error e_p for a given sector includes spatial correlations, and, if so, whether these correlations can be represented with correlation lengths, the correlations of the $SD_{s,c}$ for the three main anthropogenic sectors s are computed (Section 4.1.2). The correlations between sectors are investigated at the European and country scales. All correlations are analysed for significance and are considered significant when the p value is ≤ 0.01 . At the European scale, the correlations between sectors (hereafter named 'cross-sector correlations') are computed. For each pair of sectors (s_1, s_2) , the two sets of three maps of differences in emissions for this sector are used, that is, the series consisting of the

list of differences between pairs of inventories, in all grid cells c of the European domain:

$$\delta_{s,c}^{I} = f_{s,c}^{A} - f_{s,c}^{B} \text{ for } (I, A, B)$$

$$\in \{ (1, ED, TM), (2, ED, EC), (3, TM, EC) \}$$
 (10)

$$corr_{s_{1}, s_{2}}^{Europe} = \frac{\frac{1}{3} \frac{1}{N} \sum_{c=1}^{N} \sum_{I=1}^{3} \delta_{s_{1}, c}^{I} \delta_{s_{2}, c}^{I}}{\sqrt{\left(\frac{1}{3} \frac{1}{N} \sum_{c=1}^{N} \sum_{I=1}^{3} \delta_{s_{1}, c}^{I} 2\right) \left(\frac{1}{3} \frac{1}{N} \sum_{c=1}^{N} \sum_{I=1}^{3} \delta_{s_{2}, c}^{I} 2\right)}}$$
(11)

The same method is applied for the natural wetland emission sector. The cross-sector correlations are then represented as a matrix (Section 4.1.3).

To enable the computation of the correlations between two sectors (s_1 , s_2) and between two countries, the correlations between sectors and between countries (hereafter named 'cross-sector cross-country correlations') are obtained from two series which describe the 78 possible pairs of countries among 13 selected countries (as defined in Table 4):

$$\delta^{I}_{(s,C)} = f^{A}_{s,C} - f^{B}_{s,C}$$

for $(I,A,B) \in \{(1,ED,TM), (2,ED,EC), (3,TM,EC)\}$
and $C \in 13$ selected countries

$$(L_1, L_2)$$
 listsofcountries/ (C_a, C_b)
 $\in L_1 \times L_2$ describe the 78 pairs of countries (13)

 $corr_{s_1, s_2}^{countries}$

$$= \frac{\frac{1}{3}\frac{1}{78}\sum_{(C_a, C_b)\in(L_1\times L_2)}\sum_{I=1}^3 \delta_{(s_1, C_a)}^I \delta_{(s_2, C_b)}^I}{\sqrt{\left(\frac{1}{3}\frac{1}{78}\sum_{C_a\in L_1}\sum_{I=1}^3 \delta_{s_1, C_a}^I 2\right)\left(\frac{1}{3}\frac{1}{78}\sum_{C_b\in L_2}\sum_{I=1}^3 \delta_{s_2, C_b}^I 2\right)}}$$
(14)

The cross-sector cross-country correlations are then represented as a matrix (Section 4.1.3). Contrary to a classical correlation matrix representation, in which only pairs of sectors or pairs of countries are taken into account, the diagonal terms of the matrices in Section 4.1.3 are not equal to 1 as they represent the average correlation between pairs of countries for given sectors and are therefore always smaller than 1.

An inter-annual analysis of e_p is not possible here as the CH₄ emissions in the inventories used for this study do not vary within the year. Finally, the uncertainties of the above elements, associated to the three spatially distributed emission inventories, are evaluated by comparison to the total UNFCCC national estimates and estimates from top-down (TD) studies (Section 4.1.4).

Country	Agriculture (%)	Waste (%)	Fossil fuel related sector (%)	Wetlands (%)
AUT: Austria	29	99	54	100
BEL: Belgium	19	62	113	83
CHE: Switzerland	30	105	37	87
DEU: Germany	22	93	50	85
DNK: Denmark	29	62	48	67
ESP: Spain	28	104	48	93
FIN: Finland	48	122	124	98
FRA: France	37	83	35	101
GBR: United Kingdom	29	78	104	66
IRL: Ireland	16	99	118	94
ITA: Italy	57	80	41	77
NLD: The Netherlands	22	72	70	80
PRT: Portugal	34	58	46	95

Table 4 Standard deviation (SD) relative to the average (%) between the three anthropogenic and natural data sets for selected countries.

4. Results and discussion

4.1. Prior emission uncertainties e_p

4.1.1. Absolute values of e_p . Some studies assume e_p to be homogeneous over the whole domain or per land-use categories, for example, Bergamaschi et al. (2015) with 500% uncertainty in monthly emissions (in their free inversion setting), Tsuruta et al. (2017) with 80% over land and Thompson et al. (2017) with 50% for total emissions in the high northern latitudes. With the inventories used here, the total emissions SD is 22% and e_p depends on the location and emission sector, as shown by the large SDs (up to $5 \times 10^{-9} \,\mathrm{kg} \,\mathrm{m}^{-2} \,\mathrm{s}^{-1}$) for waste in almost all countries, for fossil fuel related sectors in some countries only (e.g. the United Kingdom, the Netherlands), for wetlands mainly in Finland, compared to low values for agriculture in almost all countries (Fig. 2g-j). The emissions in the three anthropogenic inventories differ mostly in the waste and the fossil fuel related sectors, with SDs of 58-122% and 35-124% at the national scale in the 13 selected countries (Table 4). This can be explained by the different distributions of area and point sources used for these two sectors in the three inventories. In case of wetland emissions, the SDs range between 66% and 101%, which leads to a mean SD for all 13 countries almost as high as in the waste sector (top panel of Fig. 4b). The SDs are lowest in the agriculture sector with values <58%.

The main hot-spots and high-emitting zones could be assumed to be often better known and therefore better located and specified in the inventories. This is the case for high-emitting zones such as the Netherlands or Brittany in France (Fig. 2a), where the emissions are mainly due to the agricultural sector (Fig. 2b): the spatial patterns of the three inventories are consistent (SDs $< 1.5 \times 10^{-10} \,\mathrm{kg}\,\mathrm{m}^{-2}\,\mathrm{s}^{-1}$, Fig. 2f, g). Nevertheless, some

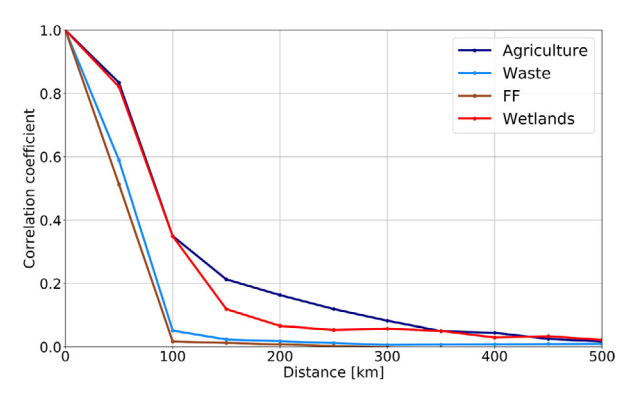
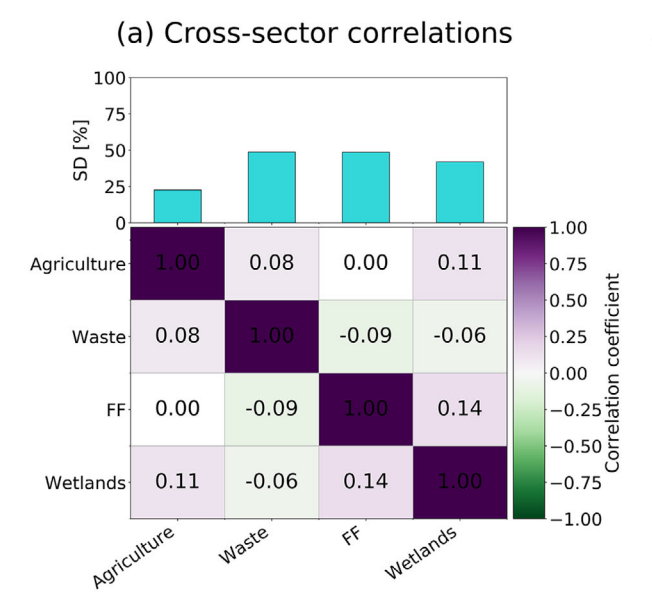


Fig. 3. Spatial correlation lengths of the prior errors for the agriculture, waste, fossil fuel (FF) related sectors and wetlands (see Section 2.2 for definition) per grid cell at the $0.5^{\circ} \times 0.5^{\circ}$ horizontal resolution.

high-emitting zones or hot-spots are not represented consistently in all three inventories: for example, the off-shore fossil fuel sector in the North Sea (Fig. 2c, h).

Differences between emission inventories are also found in low emitting areas around the coasts (Fig. 2a, f). With differences between emissions over land and sea being large, the effect of different horizontal resolutions becomes distinct at the coasts. With a CTM horizontal resolution lower than that of the inventory, land based emissions are attributed to grid cells encompassing actually land and sea areas. This problem is smaller with higher CTM horizontal resolutions. In general, the approach used for the spatial projection of emissions onto the CTM's grid impacts the patterns in the interpolated field (conservation of the mass over particular landuse categories for example) so that the interpolation method itself leads to errors. These discrepancies are a source of errors that impact specifically the assimilation



(b) Cross-sector cross-country correlations

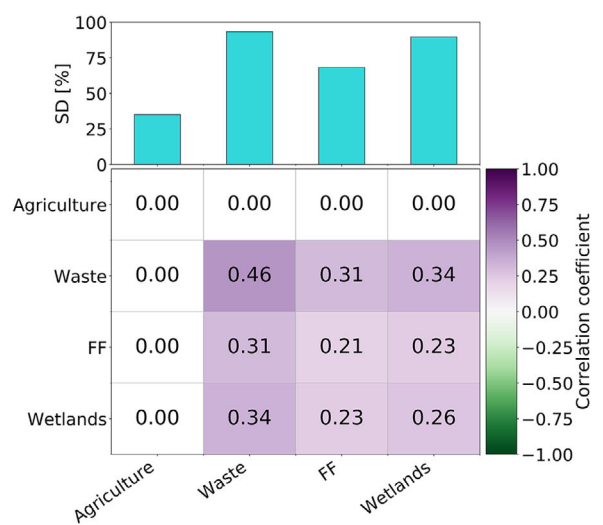


Fig. 4. Correlations (colour matrices): cross-sector correlations over the European domain (left) and cross-sector cross-country correlations for 13 selected countries (right, see Table 4 for list). White = correlation not significant, green = negative correlation, violet = positive correlation. The matching standard deviations (SD, in % of the average) are given in the top bar charts.

of data from coastal measurement sites and need to be addressed in each system.

4.1.2. Spatial correlations in e_p . The spatial correlations of the prior emission errors (Fig. 3) indicate that an exponential decay function with a correlation length of ≈100–150 km could be used to model the errors for agriculture and wetlands. For the waste sector and the fossil fuel related sectors, considering that the size of the model grid cells is approximately $50 \,\mathrm{km} \times 50 \,\mathrm{km}$, we assume that spatial correlations can be neglected. Tsuruta et al. (2019) and Bousquet et al. (2011) (inversion INV1) assumed that the errors in emissions e_p are spatially uncorrelated, which is in agreement with our analysis for the fossil fuel related sectors. In the study of Bergamaschi et al. (2015) (inversion S1), uncertainties of 100% per grid cell and month and spatial correlation scale lengths of 200 km are applied to individual emission sectors. Compared to this setting, our analysis results in a lower average uncertainty and comparable spatial correlation lengths for agriculture and waste. Theoretically, higher uncertainties and lower spatial correlation lengths give more freedom for the inversion to optimise emissions.

4.1.3. Cross-sector and cross-sector cross-country correlations in e_p . Cross-sector correlations in e_p over the whole domain are presented in Fig. 4a. These correlations are computed with a good level of statistical significance (p value <0.01) and are very weak (r<0.14), reflecting the overall independence of the sectoral emissions in the

bottom-up inventories. We also compute cross-country cross-sector correlations (Fig. 4b) for a subset of 13 countries (see country list in Table 4). The agriculture sector is correlated with no other sectors, which is consistent with the cross-sector correlations over the whole domain. However, the fossil fuel and waste sector exhibit non-negligible cross-country and cross-sector correlations (r=0.31). These small correlations are likely indirect effects of spatial correlations embedded when building the bottom-up inventories, for example when using proxies such as population density for various sectors.

4.1.4. National-scale uncertainties: comparison to estimates from other studies. National average emissions of the three anthropogenic gridded inventories and uncertainties estimated in this study are compared to emissions and uncertainties from the UNFCCC national inventory reports (NIR) for the selected 13 countries (Fig. 5). Compared to the NIRs, average emissions of the three anthropogenic gridded inventories are for most countries underestimated in the agriculture sector but overestimated in the waste and fossil fuel related sectors. However, the average country totals of the emissions of the three gridded inventories are still in the range of the NIR uncertainties, which is expected as they are constructed using similar information as the NIRs. Furthermore, the uncertainties in the NIRs are highest in the waste sector for most countries, in agreement with our estimated uncertainties. This suggests that the current knowledge of the activity data and emission factors of the waste

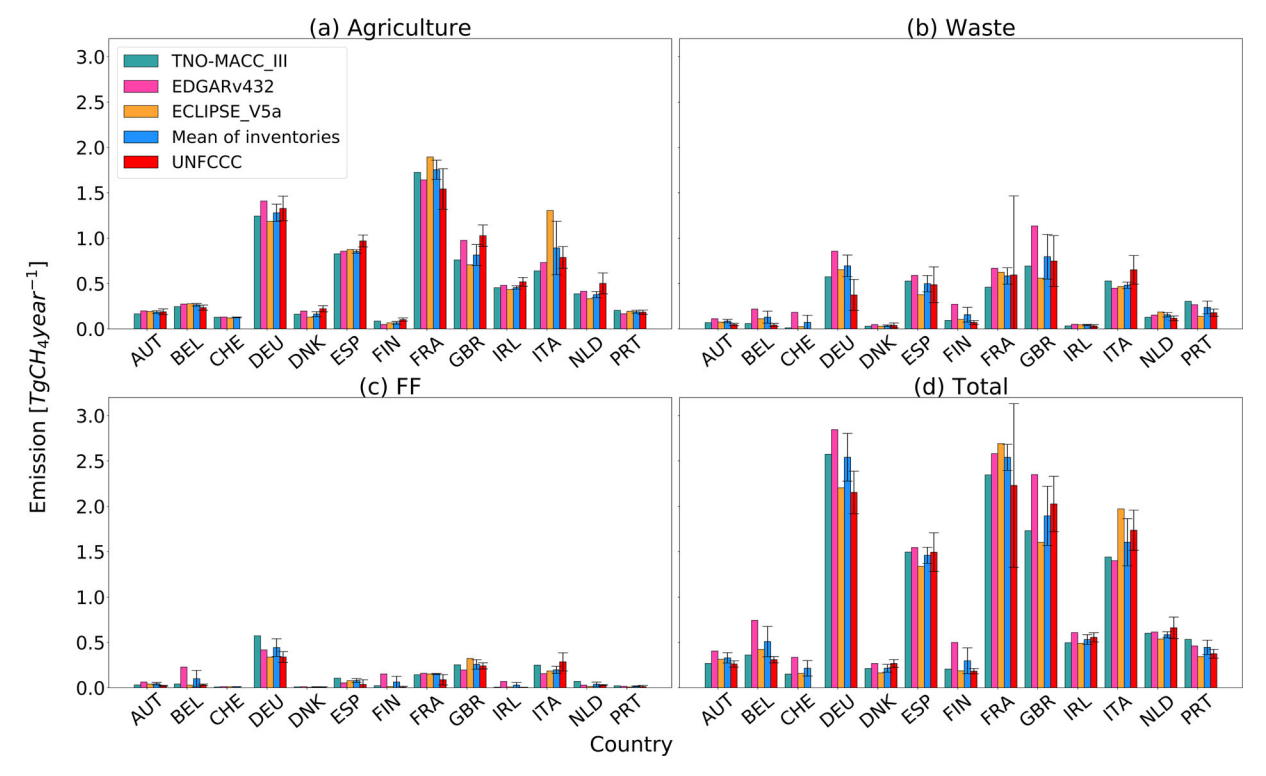


Fig. 5. Anthropogenic CH₄ emissions (Tg CH₄ year⁻¹) of different source sectors of the TNO-MACC_III (2011), EDGAR v4.3.2 (2011) and ECLIPSE V5a (2010) inventories and their average compared to the anthropogenic emissions of the UNFCCC (2016) for 13 selected countries (see Table 4 for list). The error bars indicate the uncertainties on the UNFCCC emissions and the uncertainties estimated here on the average inventory emissions. The UNFCCC emissions and corresponding uncertainties of Switzerland could not be assessed due to incomplete information in the NIR.

emission sector remains less complete than that of the agriculture and fossil fuel related sectors. To deal with the large temporal and spatial variability of the emissions in the waste sector, specific climate and operational practices should be taken into account (National Academies of Sciences, Engineering, and Medicine, 2018).

To evaluate the results of this study, a comparison to top-down estimates from other studies at the national scale is also attempted (Table 5). Unfortunately, only a few studies estimate TD emissions at national scale for the countries that we have data available for. Thus, the comparison is only possible for France (FRA, Pison et al., 2018), Finland (FIN, Tsuruta et al., 2019), the United Kingdom (GBR, Manning et al., 2011), the United Kingdom and Ireland together (GBR + IRL, Bergamaschi et al., 2010), Germany (DEU, Bergamaschi et al., 2010) and Switzerland (CHE, Henne et al., 2016). The years covered by these studies differ. However, we are mainly interested in the comparison of uncertainties and we assume that they do not vary much over the available years. For these countries, estimates are statistically consistent at $\pm 1 - \sigma$, except for France. The uncertainties reported by the TD inversion studies are larger than the uncertainties estimated in this work for the countries (except for CHE): TD uncertainties for FRA, GBR and GBR + IRL are $\sim 30\%$ larger and the ones for DEU and FIN are $\sim 2-3$ times larger. This might be due to the inversions being too conservative and using large prior errors (to give more freedom to the inversion system), which leads to large uncertainty estimates for the posterior emissions and/or this may be due to our error estimates being underestimated because of the similarities (e.g. placement of large sources) in the three inventories available for this study.

4.2. Errors in the concentration space: background error ϵ_{LBC} , representation error ϵ_{repr} , transport error ϵ_t and transported-emission error ϵ_{flx}

4.2.1. Absolute values of ε_{LBC} , ε_{repr} , ε_t and ε_{flx} . Figure 6 shows the spatial patterns of ε_{LBC} , ε_{repr} , ε_t and ε_{flx} over the domain, including the average bias, SD and the ratios of ε_{repr} , ε_t and ε_{LBC} to ε_{flx} . The annual SDs of ε_{LBC} , ε_{repr} , ε_t and ε_{flx} at the locations of the measurement sites are shown in Fig. 7. Despite of having the largest bias (3–34 ppb, Fig. 6g) compared to the biases of the

Table 5. Total anthropogenic emissions [Tg CH₄ year⁻¹] and associated uncertainties as $1-\sigma$ SD [Tg CH₄ year⁻¹ and %] from this study compared to top-down (TD) emission estimates and uncertainties from other studies and to the UNFCCC emissions and uncertainties (for country names, see Table 4).

	CHE	DEU	FIN	FRA	GBR	GBR + IRL
Our study	$0.21 \pm 0.09 (43\%)$	$2.54 \pm 0.26 \ (10\%)$	$0.30 \pm 0.14 (47\%)$	$2.54 \pm 0.14 (6\%)$	$1.89 \pm 0.33 \ (17\%)$	2.42 ± 0.61 (25%)
UNFCCC		$2.15 \pm 0.24 \ (11\%)$	$0.18 \pm 0.03 \ (16\%)$	$2.23 \pm 0.90 \ (40\%)$	$2.02 \pm 0.31 \ (15\%)$	$2.58 \pm 0.31 \ (12\%)$
TD studies	$0.2 \pm 0.02 (10\%)^{a}$	$3.67 \pm 1.25 (34\%)^{b}$	$0.31 \pm 0.34 (110\%)^{c}$	$3.9 \pm 0.31 \ (8\%)^{d}$	$1.88 \pm 0.5 (27\%)^{e}$	$3.29 \pm 1.09 (33\%)^{b}$

The UNFCCC emissions and uncertainties of Switzerland could not be assessed due to incomplete information in the NIR.

other errors, ϵ_{LBC} has the smallest and most homogeneous annual SD over Europe (15–32 ppb, Fig. 6h). This confirms that LBCs are a critical obstacle to any reliable regional inversion. Nevertheless, their uniform structure with low variability makes it possible to differentiate the LBC errors from other errors (both emission-induced and other types), and thus to optimise them in the inversion.

Patterns due to the emissions show up both in ϵ_{repr} and ϵ_t . The SD of ϵ_{repr} ranges between 1 and 80 ppb over land and reaches high values at several grid cells that contain emission hot-spots such as capitals in Europe, that is, Madrid, Paris and Warsaw. Maxima are found in high-emitting zones, such as the Silesian Coal Basin in Poland or the Po Valley in Italy (Fig. 6b). A maximum value of 80 ppb occurs in St. Petersburg. Indeed, a hot-spot of emissions appears in St. Petersburg in the total emission map of the TNO-MACC_III inventory, due to fossil fuel related emissions (see Fig. 2a and c): 54% of the total GHG emissions in St. Petersburg come from energy sources (ISAP, 2019).

The SD of ε_{repr} is in general much smaller over the sea than over the land, with values under 10 ppb, due to limited sea emissions. Nevertheless, higher values for the SD of ε_{repr} are found in the North Sea where numerous oil and gas off-shore platforms are located. The SD of ε_t ranges between 10 and 140 ppb over land. High values are found over the largest emission hot-spots and areas (Fig. 6e) rather than in areas where the transport modelling is in principle more challenging, such as coasts or mountainous zones (high values for the Alps appear only in Italy and Switzerland). The patterns in ε_{repr} and ε_{t} biases and SDs are linked to large gradients of concentrations induced by steep gradients of emissions, which have an impact even at a resolution as large as $0.5^{\circ} \times 0.5^{\circ}$. Patterns due to meteorological situations and synoptic events may occasionally generate large errors but these events are averaged out at the yearly scale studied here.

Emission hot-spots and high-emitting zones are key regions of interest for policy makers. The capacity of retrieving information on the emissions through inversions in these areas would then be particularly useful. However, the very steep spatial emission gradients encountered at scales smaller than the smallest scale used in our work (0.25°) may lead to even higher ϵ_{repr} and ϵ_t than derived here. Hence, observations near hot-spots should be used with caution within an inversion over Europe at horizontal resolutions coarser than $0.25^{\circ} \times 0.25^{\circ}$.

The SD of ϵ_{flx} ranges between 2 and 140 ppb and is the highest over grid cells where the emissions in the three inventories differ the most, for example, over the Po Valley, the Silesian Coal Basin, Istanbul (Fig. 6k). Wunch et al. (2019) have shown that there is an uncertainty in the spatial distribution of the emissions, based on the comparison of EDGAR v4.2 FT2010 (Olivier and Janssens-Maenhout, 2011) and TNO-MACC_III over parts of Europe, the differences being larger near large cities. Nevertheless, ϵ_{flx} is not necessarily the highest near large cities in our case because of the horizontal resolutions used in the simulations remain larger than the typical scale of European mega-cities.

4.2.2. Ratios of ε_{LBC} , ε_{repr} and ε_t relative to ε_{flx} . The ratios of the SDs of ε_{LBC} , ε_{repr} and ε_t relative to the SD of ε_{flx} , called hereafter $r_{SD}^{\varepsilon_{LBC}}$, $r_{SD}^{\varepsilon_{repr}}$, $r_{SD}^{\varepsilon_t}$ (Fig. 6c, f, i), are used as indicators of whether ε_{flx} dominates the other types of error. $r_{SD}^{\varepsilon_{repr}}$ is the smallest relative error at about 1 over the entire domain (Fig. 6c); $r_{SD}^{\varepsilon_{LBC}}$ and $r_{SD}^{\varepsilon_t}$ are often 2–6 (Fig. 6i, f) and therefore dominate ε_{flx} . Even though information about the statistics of these errors makes it possible to characterise them correctly, the resulting observation error matrix may be too complex due to technical limitations, for example, it is too big for the system to deal with it in an affordable computing time. In

^aHenne et al. (2016).

^bBergamaschi et al. (2010) (inversion S1, anthropogenic, average over the study years).

^cTsuruta et al. (2019) (anthropogenic).

^dPison et al. (2018) (sectoral run).

eManning et al. (2011).

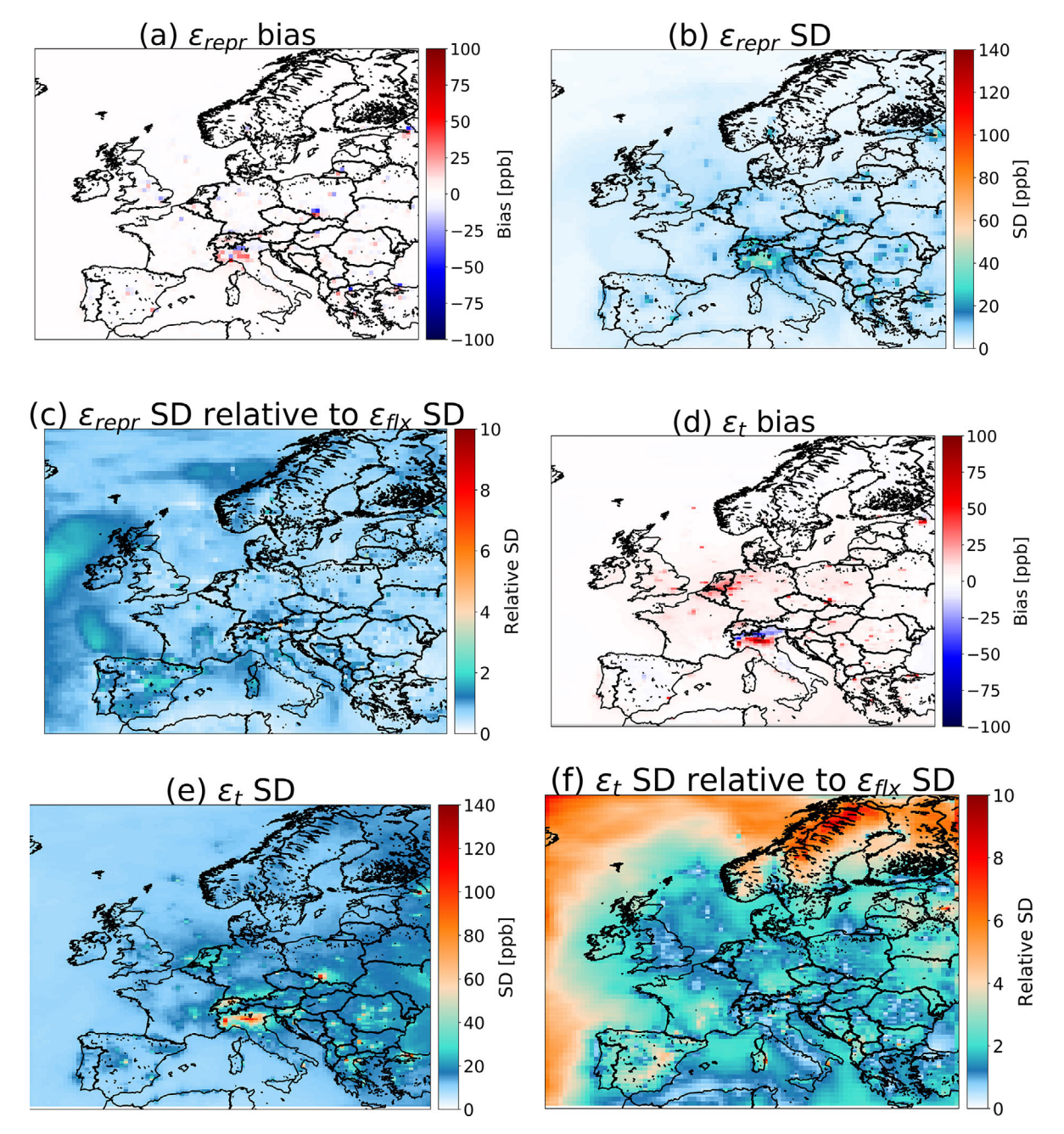


Fig. 6. Average bias (first column) and standard deviation (SD, middle column) for 2015 of (from top to bottom) ϵ_{repr} , ϵ_t , ϵ_{LBC} and ϵ_{fix} in ppb and ratios of ϵ_{repr} , ϵ_t and ϵ_{LBC} SDs to ϵ_{fix} SD. Results are shown at $0.5^{\circ} \times 0.5^{\circ}$.

this case, it is possible to include other variables, along-side the targeted emissions, in the control vector. In our case, the ratios of $\epsilon_{LBC}, \epsilon_{repr}$ and ϵ_t relative to ϵ_{flx} indicate that ϵ_{repr} could be treated in the observation error statistics whereas the sources of ϵ_{LBC} and ϵ_t may better be controlled alongside the emissions in the inversion. Including LBCs in the control vector is usually done in regional inversions, but optimising the transport

alongside emissions remains challenging in most state-ofthe-art inversion systems, although first attempts exist (e.g. Zheng et al., 2018).

4.2.3. Temporal patterns in ε_{LBC} , ε_{repr} , ε_t and ε_{flx} . Annual biases appear in ε_{LBC} , ε_{repr} , ε_t and ε_{flx} (Fig. 6g, a, d and j). As we have very few samples of errors (only three inventories), the average estimate is likely not

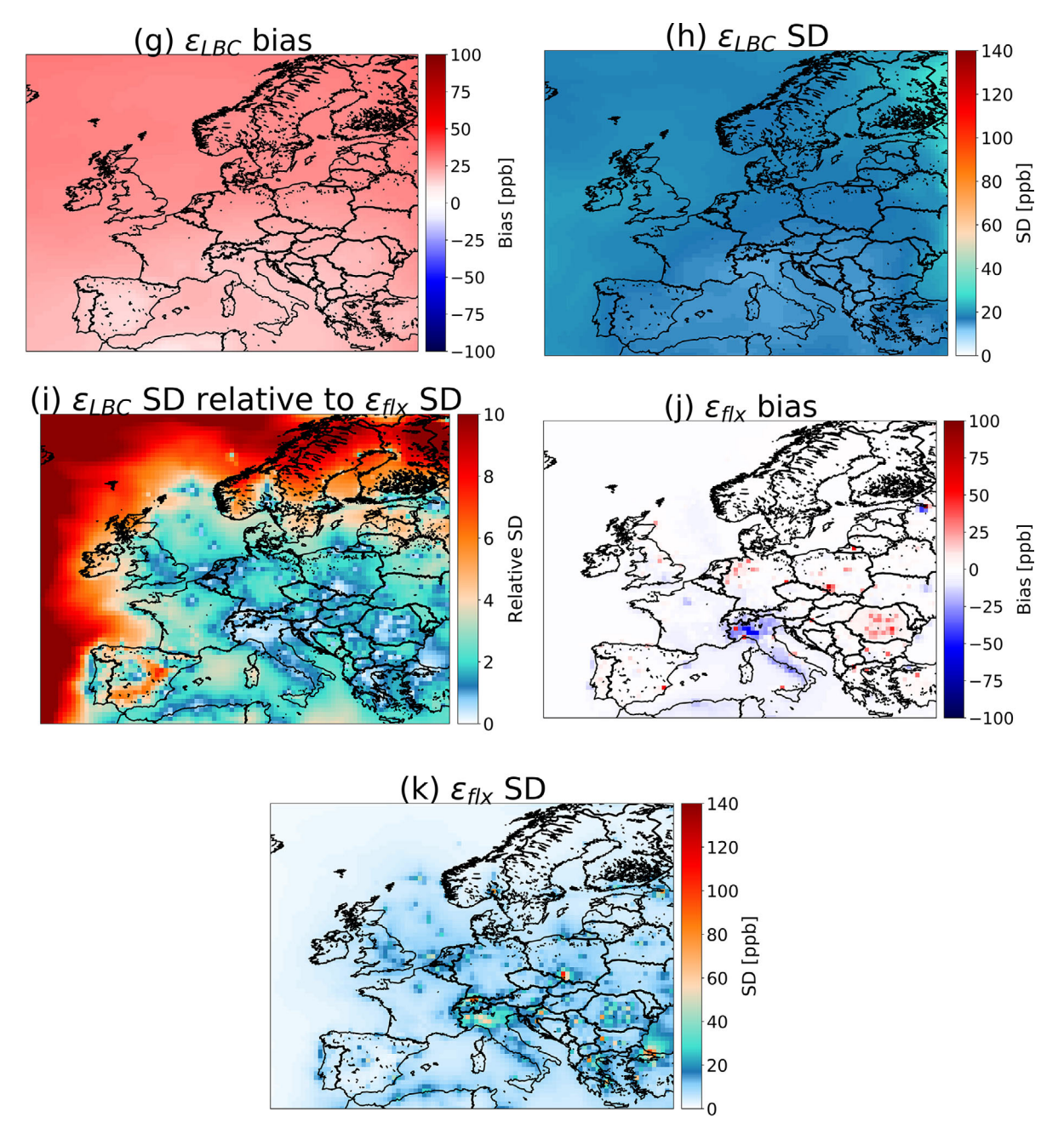


Figure 6. (Continued).

representative of an actual bias, but rather indicates strong temporal correlations of errors. ϵ_{flx} and ϵ_{repr} autocorrelations have characteristic time scales generally less than 15 days (Figs. 8 and 9), which correspond to the synoptic scale. ϵ_t scales range mainly between 5 and 50 days and ϵ_{LBC} scales are larger than one month over more than half the domain. In general, over continents, ϵ_{flx} , ϵ_{repr} and ϵ_t have similar temporal scales. The similarity of structures requires that the magnitude of ϵ_{flx} is

larger than the magnitudes of ϵ_{repr} and ϵ_t to ensure efficient filtering by the inversion system.

4.2.4. Spatial correlations in ε_{LBC} , ε_{repr} , ε_t and ε_{flx} . The average spatial correlation structures of the different errors are presented in Fig. 10. The longest characteristic scale is found for ε_{LBC} (2450 km) and the shortest for ε_{flx} (100 km) and ε_{repr} (\approx 50–100 km). The length of ε_t is intermediate (\approx 150–550 km). Lengths shorter than the

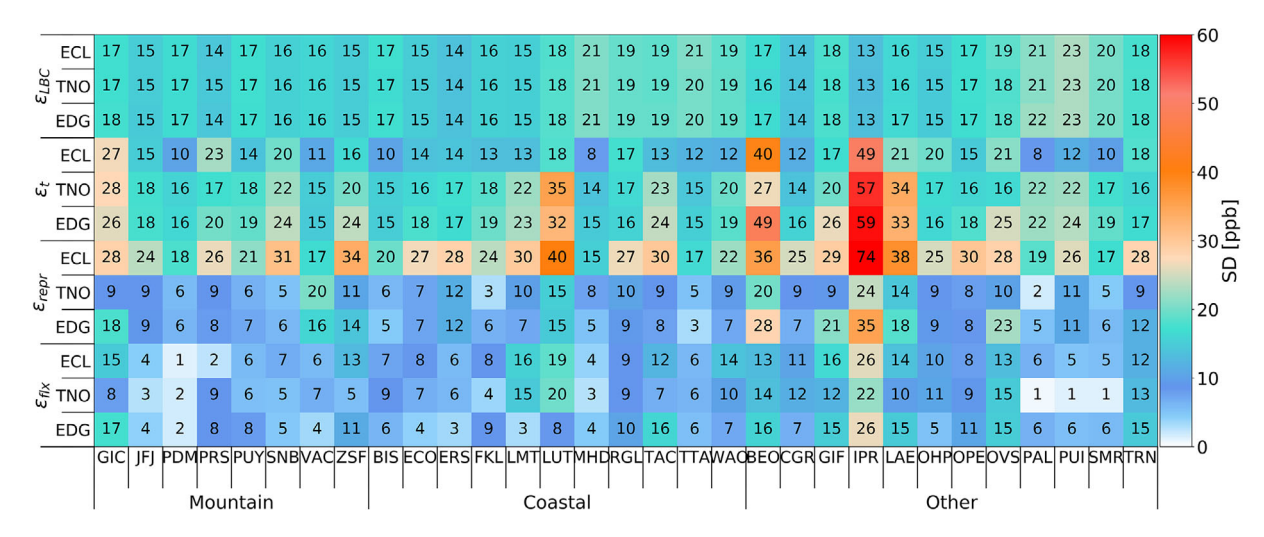


Fig. 7. Standard deviations (SDs) of ϵ_{repr} , ϵ_{tlx} and ϵ_{LBC} for 2015 at the 31 selected measurement sites (details in Table S1). The colour and number give the same information.

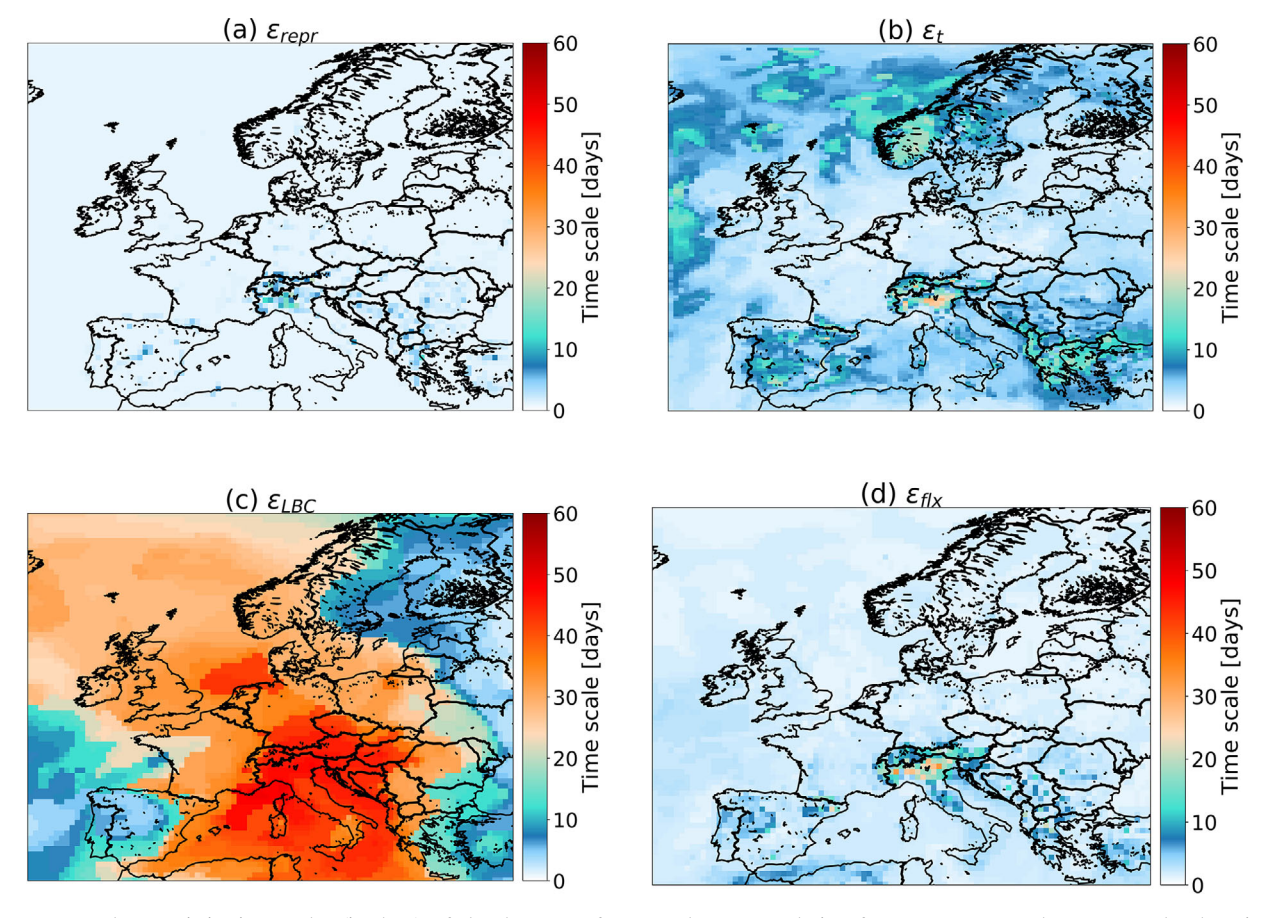


Fig. 8. Characteristic time scales (in days) of the decrease of temporal auto-correlation for ϵ_{repr} , ϵ_t , ϵ_{flx} and ϵ_{LBC} over the domain for 2015.

size of one grid cell (\approx 50 km) indicate that spatial correlations may be neglected, as is the case for ϵ_{repr} for EDGAR v4.3.2 and TNO-MACC_III. This suggests that

a network of stations with a density higher than one station per 500 km would allow an inversion system to filter LBC and transport errors as their characteristic lengths

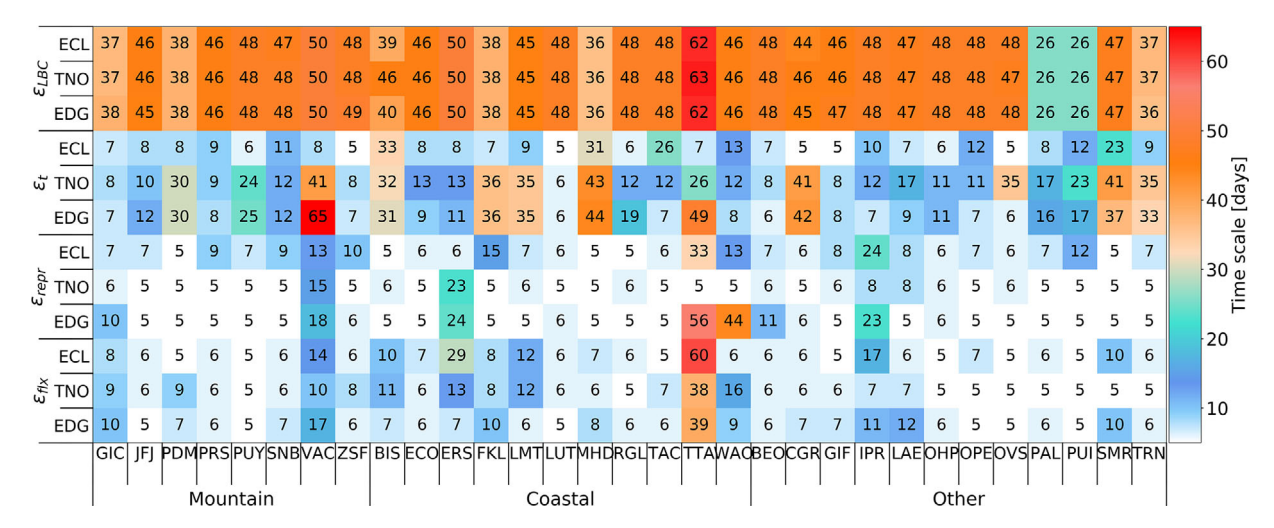


Fig. 9. Characteristic time scales (in days) of the decrease of temporal auto-correlation for ϵ_{repr} , ϵ_t , ϵ_{flx} and ϵ_{LBC} with the three inventories at the 31 selected measurement sites (details in Table S1) for 2015.

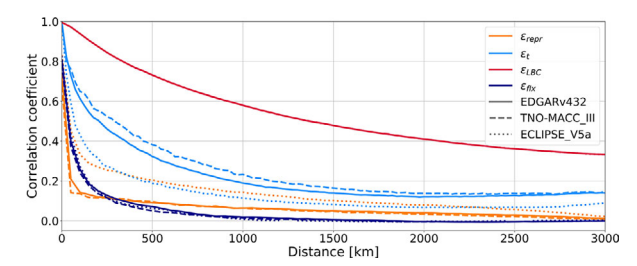


Fig. 10. Spatial correlations over the whole domain for the three estimates of ϵ_{repr} , ϵ_t and ϵ_{flx} (indicated by the name of the emission inventory used, see Section 3.2 for details) and for the estimate of ϵ_{LRC} .

are larger than 500 km with EDGAR v4.3.2 and TNO-MACC_III. However, our results show that distinguishing between representation and transported-emission errors is challenging without a very dense network (<100 km). Most of the sites used in this study are located at distances >100 km from each other, with only three groups of sites at <100 km: (i) IPR, PRS, JFJ, BEO and LAE in Switzerland and Northern Italy, (ii) GIF, OVS and TRN in France and (iii) TAC and WAO in the UK (see list of sites in Table S1).

Most studies, such as Bergamaschi et al. (2018), Tsuruta et al. (2017), Locatelli et al. (2013) or Fortems-Cheiney et al. (2012), assume the concentration errors to be spatially uncorrelated, which is not what we would recommend following our results. In our case, not taking into account correlations due to error patterns common to various measurement locations would artificially increase the weight of observations in the cost function used in the inversion and erroneously attribute all correlated patterns to the emissions. This implies that non-diagonal correlation matrices in observation states should

be used for the inversion, for which smart implementations are required. This would be more crucial in inversions using satellite data, where the main source of correlation is the uncertainties in radiative transfer inversions to obtain total column CH₄ observations. Furthermore, the spatial coverage of satellite data is more dense than data of uneven and sparse surface networks. Also, the same instrument is making the measurements. For these reasons, error correlations in space and/ or time may occur and necessitate to account for offdiagonal terms in the observation variance-covariance matrix. This could be crucial, especially for instruments with a large swath and short revisit time, producing a lot of neighbouring data. Since satellite data are vertically integrated, the here presented errors may differ and should thus be recomputed when using satellite data for inversions.

4.2.5. Total concentration errors. The total concentration errors at the domain scale range between 14 and 422 ppb, with an average of 29 ppb, and between 21 and 53 ppb at the measurement site locations (see Table 6). The total values per site category are similar with averages of 43 ppb, 40 ppb and 42 ppb for coastal, mountain and 'other' sites. The total concentration errors at the Swiss sites BEO, JFJ and LAE can be compared to the ones used in the study of Henne et al. (2016). The total error for BEO and LAE (called LHW in Henne et al. 2016) with 38 and 46 ppb, respectively, compare well with the ranges of total errors of 1-41 ppb for BEO and 14-44 ppb for LAE in the different inversion set-ups in Henne et al. (2016). For JFJ, our estimate of 46 ppb is higher than 14-20 ppb in their study. Ranges for combined measurement and model errors for CH4 are also

reported in the study of Bergamaschi et al. (2015). Our estimates are in the lower range of their set-ups with the LMDz-4DVAR (3–450 ppb) and TM5-4DVAR (3–1000 ppb) inversion systems and above the range of 10–30 ppb with TM3-STILT (except for GIC with 21 ppb).

5. Conclusions and recommendations

This study aims at estimating errors that need to be taken into account in atmospheric inversions of CH₄ emissions at the European scale. We have used a simple (i.e. technically ready and not expensive in computing time) and easy to update method that consists of performing a set of simulations using two limited-area CTMs at three different horizontal resolutions with inputs based on three anthropogenic emission inventories, three data sets of natural emissions and two sets of boundary and initial conditions. The analysis presented here can be applied for any atmospheric species and extended to any other region as long as the required components (sufficient number of emission inventories, multiple CTMs and LBC products) are available. For example, the USA or China would be a good option as the required components are available for them.

We have performed the analysis for the year 2015. Four types of errors have been estimated by computing differences of simulated hourly mixing ratios:

- the background error ε_{LBC}, due to the lateral boundary and initial conditions used by the area-limited CTMs;
- the representation error ε_{repr} , due to the difference of representativity between a model's grid-cell and atmospheric mixing ratio measurements;
- the transport error ε_t, due to discretisation, parametrisations of the fundamental equations of the atmospheric transport used in a model and to the meteorological inputs used by the CTMs;
- the transported-emission error ε_{flx} , due to the misrepresentation of emissions on the spatial and temporal grid of the model.

To be consistent with the usual choice of data based on expert knowledge, the errors have been computed from afternoon values (13–17 h UTC included) for non-mountain sites and from night-time values (00–04 h UTC included) for mountain sites, either in all the first-model-layer grid cells of the European domain or at the locations (horizontal and vertical grid cell) of 31 selected measurement sites. We have shown that this choice is not always optimal depending on stations and that it should be reassessed by inverse modellers (e.g. by using a

Table 6. Total errors [ppb] in the concentration space at the location of measurement sites (see more information on sites and locations in Table S1 and in Fig. 1).

Trigram of site	Total concentration errors
Mountain sites	
GIC	21
JFJ	46
PDM	43
PRS	52
PUY	37
SNB	41
VAC	41
ZSF	37
Coastal sites	
BIS	39
ECO	45
ERS	46
FKL	50
LMT	48
LUT	31
MHD	40
RGL	40
TAC	42
TTA	45
WAO	47
Other sites	
BEO	38
CGR	46
GIF	39
IPR	37
LAE	34
OHP	45
OPE	38
OVS	39
PAL	50
PUI	53
SMR	49
TRN	37

method similar to the one described in Sections 3.4 and S3).

The methodology used in this study to estimate errors is specific to our set-up of CHIMERE (coarse horizontal resolution, chosen inputs) for continental scale CH₄ emissions using a set of *in situ* monitoring sites. Nevertheless, the obtained error estimates allow us to gain insights into how these errors could be treated in a data assimilation system for inverting CH₄ emissions at the European scale, as summarised in Table 7:

• ϵ_{LBC} appears to be simple to take into account because of its uniform structure with low variability, which makes it possible to differentiate it from the other errors. ϵ_{LBC} can be considered as a parameter

Table 7. Summary of the errors estimated in this study: main recommendations to treat each error in an inversion system for targeting
CH ₄ emissions in Europe at the yearly scale and orders of magnitude of correlation lengths which can be used to simply represent
some of them.

Error	Magnitude relative to ϵ_{flx}	Recommended treatment	Temporal correlation lengths	Spatial correlation lengths
ϵ_{flx}	1	controlled (emissions are the main target of the inversion)	<15 days (due to meteorology, other sources of error in time not accounted for)	≈100 km
$\epsilon_{ m repr}$	≈1	In the observation statistics	<15 days	None
ϵ_{t}	2-6	Controlled alongside the emissions	5-50 days	150–550 km
ϵ_{LBC}	2–6	Controlled or in the prior statistic or pre-treated	>1 month	>2400 km
$e_{ m p}$	Not studied	In the prior statistics	Not accounted for	Agriculture: 100–150km for other sectors: negligible
			Other correlations: cross-sect fossil fuel related & waste Cross-sector cross-country fo	tor agriculture & waste;

to invert or could even be corrected beforehand. The relative magnitude of ϵ_{LBC} compared to ϵ_{flx} indicates that, in the inversion framework, the sources of ϵ_{LBC} may better be controlled alongside the emissions. This is consistent with what is usually done in regional inversions, which include lateral boundary and initial conditions in their control vector. At the scale studied here, long temporal (>1 month) and spatial (>2400 km) correlation lengths could be used to represent ϵ_{LBC} .

- $\varepsilon_{\rm repr}$ and $\varepsilon_{\rm t}$ may be underestimated in our set of simulations close to hot-spots and high-emitting zones. This is due to the horizontal resolutions used for the simulations being coarser than the scale at which CH₄ emission patterns actually vary. Steep gradients of concentrations induced by steep gradients of emissions encountered in certain types of activity sectors (e.g. waste) can, therefore, not be represented well in our models' configurations. Even though hot-spots and high-emitting zones are key regions for policy makers, in which a reduction of uncertainties on emissions brought by the inversions would be very useful, our study shows that observations near these areas should be used with caution with horizontal resolutions coarser than $0.25^{\circ} \times 0.25^{\circ}$. The relative magnitudes of ϵ_{repr} and ϵ_t compared to ϵ_{flx} indicate that ε_{repr} can be treated in the inversion within the observation error statistics whereas the sources of ε_t may better be controlled alongside the emissions in
- the inversion. Nevertheless, optimising transport characteristics at the same time as emissions remains challenging in most state-of-the-art inversion systems. Moreover, spatial (from 150 to $550\,\mathrm{km}$ depending on the prior inventory) and temporal (from 5 to 50 days) correlation lengths would have to be used for ϵ_t , which may be an issue because of the technical challenge of inverting non-diagonal large matrices.
- ϵ_{flx} may be represented by short spatial correlation lengths ($\approx 100 \, km$, i.e. twice our coarsest resolution). Since emissions do not vary through the year in the inventories used here, temporal aggregation errors could not be studied and temporal patterns in ϵ_{flx} are only due to meteorology. In this case, the use of short temporal correlation lengths (<15 days) is recommended.

The spatial correlation lengths estimated here show that some error patterns cover a number of measurement sites, whereas errors in *in situ* fixed measurements are generally assumed to be uncorrelated in inversion systems.

Moreover, we have estimated the error in the emission inventories, $e_{\rm p}$, particularly at the country and sector (agriculture, waste, fossil fuel related emissions and wetlands) scales as atmospheric inversions require prior emission errors in their statistics of the emission space. Due to the assumptions and proxies used for the spatial distribution of area and point sources in the inventories, they

differ the most for the waste and fossil fuel related sectors and agree better for agriculture at the European scale. The disagreements are particularly due to some highemitting zones or hot-spots not being represented consistently, that is, their locations and/or emissions vary between the three inventories. Discrepancies also arise from the projection of emissions onto the model's grid along the coasts, which may impact specifically the assimilation of data from coastal measurement sites. All cases where emission gradients between two neighbouring types of land-use are steep will lead to such an issue. Spatial correlation lengths that are recommended to represent e_p for agricultural emissions are $\approx 100-150$ km. Cross-sector and cross-sector cross-country correlations show the impact of spatial correlations that are used in the inventories. Our simple analysis based on the available inventories indicates that errors are heterogeneous and depend on the sector and country, which is in contrast with most inversion studies where the assumed uncertainties are homogeneous, with only land being different from sea. Finally, there is a need for an in-depth analysis and/or update of the spatial distribution of current emission inventories and for a more complete error estimation study dedicated to emission inventories.

Following the method chosen here, further work should target the following:

- ε_{repr} and ε_t should be analysed on finer horizontal resolutions, mainly with the objective of assimilating satellite imagery.
- ε_t should be further analysed with different meteorological inputs, particularly to investigate the vertical mixing representation, which is known as a large source of error (Dabberdt et al., 2004; Locatelli et al., 2015).
- εfix and ep could be improved by adding simulations based on other emission inventories; either including new inventories that may become available, or the same inventories with added features such as seasonal or hourly time profiles. Although natural emissions are small compared to anthropogenic contributions in Europe, they are not negligible everywhere, particularly in northern regions dominated by natural wetlands. Errors of natural emissions other than wetlands could be studied with the same methodology as the anthropogenic and wetland emissions.

Acknowledgements

We are grateful to the colleagues at TNO for their valuable support. We thank Matthew Lang, Diego Santaren and Audrey Fortems-Cheiney for their helpful advice. Calculations were performed using the resources of LSCE, maintained by François Marabelle and the LSCE IT team. We thank the PIs of the measurement sites we used in this study for maintaining methane measurements and for sharing their data through the following contributors: World Data Centre Greenhouse Gases (WDCGG), Institut Català Ciències del Clima (IC3), Swiss Federal Laboratories for Materials Science and Technology (Empa), Laboratoire des Sciences du Climat et de l'Environnement (LSCE), Ricerca sul Sistema Energetico (RSE), Integrated non-CO2 Greenhouse gas Observing System (InGOS), Integrated Carbon Observation System Umweltbundesamt (UBA), Environmental Chemical Process Laboratory (ECPL), National Oceanic and Atmospheric Administration (NOAA) Earth System Research Laboratories (ESRL), University of Bristol, Norwegian Institute for Air Research (NILU), University of Bern, Joint Research Centre (JRC), Observatoire des Sciences de l'Univers Institut Pythéas (OSU), Finnish Institute (FMI), Meteorological and of Helsinki.

Disclosure statement

The authors declare no competing interests.

Funding

This project is part of the MEMO² (MEthane goes MObile – MEasurements and MOdelling) project and has received funding from the European Unions Horizon 2020 research and innovation programme under the Marie Sklodowska-Curie Grant Agreement No. 722479. Ana Maria Roxana Petrescu acknowledges the support of the European Unions Horizon 2020 VERIFY project, Grant No. 776810.

Data availability statement

The data that support the findings of this study are available from the corresponding author upon request.

Supplemental data

Supplemental data for this article can be accessed here.

References

Arora, V. K., Melton, J. R. and Plummer, D. 2018. An assessment of natural methane fluxes simulated by the

- CLASS-CTEM model. *Biogeosciences* **15**, 4683–4709. https://bg.copernicus.org/articles/15/4683/2018/.
- Berchet, A., Pison, I., Chevallier, F., Bousquet, P., Bonne, J.-L. and co-authors. 2015. Objectified quantification of uncertainties in Bayesian atmospheric inversions. *Geosci. Model Dev.* **8**, 1525–1546. https://www.geosci-model-dev.net/8/1525/2015/.
- Bergamaschi, P., Corazza, M., Karstens, U., Athanassiadou, M., Thompson, R. and co-authors. 2015. Top-down estimates of European CH₄ and N₂O emissions based on four different inverse models. *Atmos. Chem. Phys.* **15**, 715–736. doi:10.5194/acp-15-715-2015
- Bergamaschi, P., Karstens, U., Manning, A. J., Saunois, M., Tsuruta, A. and co-authors. 2018. Inverse modelling of European CH₄ emissions during 2006–2012 using different inverse models and reassessed atmospheric observations. *Atmos. Chem. Phys.* 18, 901–920. https://www.atmos-chemphys.net/18/901/2018/.
- Bergamaschi, P., Krol, M., Dentener, F., Vermeulen, A., Meinhardt, F. and co-authors. 2005. Inverse modelling of national and European CH₄ emissions using the atmospheric zoom model TM5. Atmos. Chem. Phys. 5, 2431–2460. https:// www.atmos-chem-phys.net/5/2431/2005/.
- Bergamaschi, P., Krol, M., Meirink, J. F., Dentener, F., Segers, A. and co-authors. 2010. Inverse modeling of European CH₄ emissions 2001–2006. *J. Geophys. Res.: Atmos.* 115, D22309. https://agupubs.onlinelibrary.wiley.com/doi/abs/10.1029/ 2010JD014180.
- Bocquet, M., Wu, L., and Chevallier, F. 2011. Bayesian design of control space for optimal assimilation of observations. Part I: Consistent multiscale formalism. Q. J. R Meteorolog. Soc. 137, 1340–1356. https://rmets.onlinelibrary.wiley.com/doi/abs/ 10.1002/qj.837.
- Bousquet, P., Ciais, P., Miller, J. B., Dlugokencky, E. J., Hauglustaine, D. A. and co-authors. 2006. Contribution of anthropogenic and natural sources to atmospheric methane variability. *Nature* 443, 439–443. doi:10.1038/nature05132
- Bousquet, P., Pierangelo, C., Bacour, C., Marshall, J., Peylin, P. and co-authors. 2018. Error budget of the methane remote Lidar mission and its impact on the uncertainties of the global methane budget. *Journal of Geophysical Research: Atmospheres* 123, 11,766–11,785. https://agupubs.onlinelibrary.wiley.com/doi/abs/10.1029/2018JD028907.
- Bousquet, P., Ringeval, B., Pison, I., Dlugokencky, E. J., Brunke, E.-G. and co-authors. 2011. Source attribution of the changes in atmospheric methane for 2006–2008. *Atmos. Chem. Phys.* 11, 3689–3700. https://www.atmos-chem-phys.net/11/3689/2011/.
- Broquet, G., Chevallier, F., Rayner, P., Aulagnier, C., Pison, I. and co-authors. 2011. A European summertime CO₂ biogenic flux inversion at mesoscale from continuous in situ mixing ratio measurements. *J. Geophys. Res.: Atmos.* **116**, D23303. https://agupubs.onlinelibrary.wiley.com/doi/abs/10.1029/2011JD016202
- Dabberdt, W., Carroll, M., Baumgardner, D., Carmichael, G., Cohen, R. and co-authors. 2004. Meteorological research needs for improved air quality forecasting: report of the 11th

- prospectus development team of the U.S. Weather Research Program. *Bull. Amer. Meterol. Soc.* **85**, 563. doi:10.1175/BAMS-85-4-563
- EEA. 2019. Annual European Union greenhouse gas inventory 1990–2017 and inventory report 2019. https://www.eea.europa.eu/publications/european-union-greenhouse-gas-inventory-2019.
- Fortems-Cheiney, A., Chevallier, F., Pison, I., Bousquet, P., Saunois, M. and co-authors. 2012. The formaldehyde budget as seen by a global-scale multi-constraint and multi-species inversion system. *Atmos. Chem. Phys.* 12, 6699–6721. https://www.atmos-chem-phys.net/12/6699/2012/.
- Fortems-Cheiney, A., Pison, I., Dufour, G., Broquet, G., Berchet, A. and co-authors. 2019. Variational regional inverse modeling of reactive species emissions with PYVAR-CHIMERE. *Geosci. Model Dev. Discuss.* 2019, 1–22. https://www.geosci-model-dev-discuss.net/gmd-2019-186/.
- Ganesan, A. L., Rigby, M., Zammit-Mangion, A., Manning, A. J., Prinn, R. G. and co-authors. 2014. Characterization of uncertainties in atmospheric trace gas inversions using hierarchical Bayesian methods. *Atmos. Chem. Phys.* 14, 3855–3864. https://www.atmos-chem-phys.net/14/3855/2014/.
- Hayman, G. D., O'Connor, F. M., Dalvi, M., Clark, D. B., Gedney, N. and co-authors. 2014. Comparison of the HadGEM2 climate–chemistry model against in situ and SCIAMACHY atmospheric methane data. *Atmos. Chem. Phys.* 14, 13257–13280. https://acp.copernicus.org/articles/14/ 13257/2014/.
- Henne, S., Brunner, D., Oney, B., Leuenberger, M., Eugster, W. and co-authors. 2016. Validation of the Swiss methane emission inventory by atmospheric observations and inverse modelling. Atmos. Chem. Phys. 16, 3683–3710. https://www.atmos-chem-phys.net/16/3683/2016/.
- Hourdin, F., Musat, I., Bony, S., Braconnot, P., Codron, F. and co-authors. 2006. The LMDZ4 general circulation model: climate performance and sensitivity to parametrized physics with emphasis on tropical convection. *Clim. Dyn.* 27, 787–813. doi:10.1007/s00382-006-0158-0
- Hu, H., Landgraf, J., Detmers, R., Borsdorff, T., Aan de Brugh, J. and co-authors. 2018. Toward global mapping of methane with TROPOMI: first results and intersatellite comparison to GOSAT. *Geophys. Res. Lett.* 45, 3682–3689. https://agupubs.onlinelibrary.wiley.com/doi/abs/10.1002/2018GL077259.
- IPCC. 2013. Summary for policymakers. In: Climate Change 2013: The Physical Science Basis. Contribution of Working Group I to the Fifth Assessment Report of the Intergovernmental Panel on Climate Change (ed. T. F. Stocker, D. Qin, G.-K. Plattner, M. Tignor, S. K. Allen, J. Boschung, A. Nauels, Y. Xia, V. Bex and P. M. Midgley), Cambridge, United Kingdom and New York, NY, USA. Cambridge University Press, pp. 1–30. www.climatechange2013.org.
- IPCC. 2006. IPCC Guidelines for National Greenhouse Gas Inventories, Prepared by the National Greenhouse Gas Inventories Programme (ed. H. S. Eggleston, L. Buendia, K. Miwa, T. Ngara and K. Tanabe). Institute for Global Environmental Strategies, Japan.

- ISAP. 2019. Integrated Sustainability Action Plan. http://www.stpete.org/sustainability/integrated_sustainability_action_plan.php.
- Janssens-Maenhout, G., Crippa, M., Guizzardi, D., Muntean, M., Schaaf, E. and co-authors. 2019. EDGAR v4.3.2 Global Atlas of the three major greenhouse gas emissions for the period 1970–2012. Earth Syst. Sci. Data 11, 959–1002. https://essd.copernicus.org/articles/11/959/2019/.
- Jonas, M., Marland, G., Winiwarter, W., White, T., Nahorski, Z. and co-authors. 2011. Benefits of dealing with uncertainty in greenhouse gas inventories: introduction. In: Greenhouse Gas Inventories: Dealing with Uncertainty, Springer Netherlands, Dordrecht, pp. 3–18. https://doi.org/10.1007/978-94-007-1670-4 2.
- Kaminski, T., Rayner, P., Heimann, M., and and Enting, I. 2001. On aggregation errors in atmospheric transport inversion. J. Geophys. Res. 106, 4703–4715. doi:10.1029/ 2000JD900581
- Koffi, E., Bergamaschi, P., Karstens, U., Krol, M., Segers, A. J. and co-authors. 2016. Evaluation of the boundary layer dynamics of the TM5 model. *Geosci. Model Dev. Discuss.* 9, 1–37.
- Kuenen, J. J. P., Visschedijk, A. J. H., Jozwicka, M. and Denier van der Gon, H. A. C. 2014. TNO-MACC_II emission inventory; a multi-year (2003–2009) consistent high-resolution European emission inventory for air quality modelling. *Atmos. Chem. Phys.* 14, 10963–10976. https://www.atmoschem-phys.net/14/10963/2014/.
- Locatelli, R., Bousquet, P., Chevallier, F., Fortems-Cheney, A., Szopa, S. and co-authors. 2013. Impact of transport model errors on the global and regional methane emissions estimated by inverse modelling. *Atmos. Chem. Phys.* 13, 9917–9937. https://www.atmos-chem-phys.net/13/9917/2013/.
- Locatelli, R., Bousquet, P., Hourdin, F., Saunois, M., Cozic, A. and co-authors. 2015. Atmospheric transport and chemistry of trace gases in LMDz5B: evaluation and implications for inverse modelling. *Geosci. Model Dev.* 8, 129–150. https://gmd.copernicus.org/articles/8/129/2015/.
- Lunt, M. F., Rigby, M., Ganesan, A. L. and Manning, A. J. 2016. Estimation of trace gas fluxes with objectively determined basis functions using reversible-jump Markov chain Monte Carlo. Geosci. Model Dev. 9, 3213–3229. https:// www.geosci-model-dev.net/9/3213/2016/.
- Mailler, S., Menut, L., Khvorostyanov, D., Valari, M., Couvidat, F. and co-authors. 2017. CHIMERE-2017: from urban to hemispheric chemistry-transport modeling. *Geosci. Model Dev.* 10, 2397–2423. https://www.geosci-model-dev.net/ 10/2397/2017/.
- Manders, A., Builtjes, P. J. H., Curier, L., Denier van der Gon, H., Hendriks, C. and co-authors. 2017. Curriculum vitae of the LOTOS-EUROS (v2.0) chemistry transport model. *Geosci. Model Dev. Discuss.* 10, 1–53.
- Manning, A. J., Doherty, S., O' Jones, A. R., Simmonds, P. G. and Derwent, R. G. 2011. Estimating UK methane and nitrous oxide emissions from 1990 to 2007 using an inversion modeling approach. J. Geophys. Res.: Atmos. 116, D02305. https://agupubs. onlinelibrary.wiley.com/doi/abs/10.1029/2010JD014763.

- Marécal, V., Peuch, V.-H., Andersson, C., Andersson, S., Arteta, J. and co-authors. 2015. A regional air quality forecasting system over Europe: the MACC-II daily ensemble production. *Geosci. Model Dev.* 8, 2777–2813. https://www.geosci-model-dev.net/8/2777/2015/.
- McNorton, J., Bousserez, N., Agustí-Panareda, A., Balsamo, G., Choulga, M. and co-authors. 2020. Representing model uncertainty for global atmospheric CO₂ flux inversions using ECMWF-IFS-46R1. *Geosci. Model Dev. Discuss.* **2020**, 1–30. https://www.geosci-model-dev-discuss.net/gmd-2019-314/.
- Menut, L., Bessagnet, B., Khvorostyanov, D., Beekmann, M., Blond, N. and co-authors. 2013. CHIMERE 2013: a model for regional atmospheric composition modelling. *Geosci. Model Dev.* 6, 981–1028. https://www.geosci-model-dev.net/6/981/2013/.
- National Academies of Sciences, Engineering, and Medicine. 2018. Improving Characterization of Anthropogenic Methane Emissions in the United States, 4 Addressing Uncertainties in Anthropogenic Methane Emissions. The National Academies Press, Washington, DC. https://www.ncbi.nlm.nih.gov/books/ NBK519298/.
- Olivier, J. and Janssens-Maenhout, G. 2011. Part III: greenhouse gas emissions. In: *CO2 emissions from fuel combustion*. Paris (France): International Energy Agency (IEA). https://publications.jrc.ec.europa.eu/repository/handle/JRC67519.
- Peltola, O., Vesala, T., Gao, Y., Räty, O., Alekseychik, P. and co-authors. 2019. Monthly gridded data product of northern wetland methane emissions based on upscaling eddy covariance observations. *Earth Syst. Sci. Data* 11, 1263–1289. https://www.earth-syst-sci-data.net/11/1263/2019/.
- Pison, I., Berchet, A., Saunois, M., Bousquet, P., Broquet, G. and co-authors. 2018. How a European network may help with estimating methane emissions on the French national scale. *Atmos. Chem. Phys.* 18, 3779–3798. https://www.atmoschem-phys.net/18/3779/2018/.
- Ringeval, B., de Noblet-Ducoudré, N., Ciais, P., Bousquet, P., Prigent, C. and co-authors. 2010. An attempt to quantify the impact of changes in wetland extent on methane emissions on the seasonal and interannual time scales. *Global Biogeochem. Cycles* 24, GB2003. https://agupubs.onlinelibrary.wiley.com/ doi/abs/10.1029/2008GB003354.
- Ringeval, B., Friedlingstein, P., Koven, C., Ciais, P., de Noblet, N. and co-authors. 2011. Climate-CH₄ feedback from wetlands and its interaction with the climate-CO₂ feedback. *Biogeosciences* 8, 2137–2157. doi:10.5194/bg-8-2137-2011
- Saunois, M., Bousquet, P., Poulter, B., Peregon, A., Ciais, P. and co-authors. 2016a. The global methane budget 2000–2012. *Earth Syst. Sci. Data* **8**, 697–751. https://www.earth-syst-sci-data.net/8/697/2016/.
- Saunois, M., Jackson, R. B., Bousquet, P., Poulter, B. and Canadell, J. G. 2016b. The growing role of methane in anthropogenic climate change. *Environ. Res. Lett.* 11, 120207. doi:10.1088/1748-9326/11/12/120207
- Segers, A. and Houweling, S. Description of the CH₄ Inversion Production Chain. ECMWF Copernicus Report, 2017. URL https://atmosphere.copernicus.eu/sites/default/files/2020-01/

- CAMS73_2018SC1_D73.5.2.2-2019_202001_production_chain_v1.pdf.
- Stohl, A., Aamaas, B., Amann, M., Baker, L. H., Bellouin, N. and co-authors. 2015. Evaluating the climate and air quality impacts of short-lived pollutants. *Atmos. Chem. Phys.* 15, 10529–10566. https://www.atmos-chem-phys.net/15/10529/2015/.
- Tarantola, A. 2005. Inverse Problem Theory and Methods for Model Parameter Estimation. Society for Industrial and Applied Mathematics, Philadelphia, PA.
- Thompson, R. L., Sasakawa, M., Machida, T., Aalto, T., Worthy, D. and co-authors. 2017. Methane fluxes in the high northern latitudes for 2005–2013 estimated using a Bayesian atmospheric inversion. *Atmos. Chem. Phys.* 17, 3553–3572. https://www.atmos-chem-phys.net/17/3553/2017/.
- Thompson, R. L., Stohl, A., Zhou, L. X., Dlugokencky, E., Fukuyama, Y. and co-authors. 2015. Methane emissions in East Asia for 2000–2011 estimated using an atmospheric Bayesian inversion. *J. Geophys. Res.: Atmos.* 120, 4352–4369. https://agupubs.onlinelibrary.wiley.com/doi/abs/10.1002/2014JD022394.
- Tsuruta, A., Aalto, T., Backman, L., Hakkarainen, J., van der Laan-Luijkx, I. T. and co-authors. 2017. Global methane emission estimates for 2000–2012 from CarbonTracker Europe-CH₄ v1.0. Geosci. Model Dev. 10, 1261–1289. https:// www.geosci-model-dev.net/10/1261/2017/.
- Tsuruta, A., Aalto, T., Backman, L., Krol, M. C., Peters, W. and co-authors. 2019. Methane budget estimates in Finland

- from the CarbonTracker Europe-CH4 data assimilation system. *Tellus B: Chem. Phys. Meteorol.* **71**, 1–20. https://doi.org/10.1080/16000889.2018.1565030.
- Varon, D. J., McKeever, J., Jervis, D., Maasakkers, J. D., Pandey, S. and co-authors. 2019. Satellite discovery of anomalously large methane point sources from oil/gas production. *Geophys. Res. Lett.* 46, 13507–13516. https://agupubs.onlinelibrary.wiley.com/doi/abs/10.1029/2019GL083798.
- Wang, F., Maksyutov, S., Tsuruta, A., Janardanan, R., Ito, A. and co-authors. 2019. Methane emission estimates by the global high-resolution inverse model using national inventories. *Remote Sensing* 11, 2489. https://www.mdpi.com/2072-4292/11/21/2489.
- Wang, Y., Broquet, G., Ciais, P., Chevallier, F., Vogel, F. and co-authors. 2017. Estimation of observation errors for largescale atmospheric inversion of CO₂ emissions from fossil fuel combustion. *Tellus B: Chem. Phys. Meteorol.* 69, 1325723. doi:10.1080/16000889.2017.1325723
- Wunch, D., Jones, D. B. A., Toon, G. C., Deutscher, N. M., Hase, F. and co-authors. 2019. Emissions of methane in Europe inferred by total column measurements. *Atmos. Chem. Phys.* 19, 3963–3980. https://www.atmos-chem-phys.net/19/3963/2019/. doi:10.5194/acp-19-3963-2019
- Zheng, T., French, N. H. F., and and Baxter, M. 2018. Development of the WRF-CO2 4D-Var assimilation system v1.0. Geosci. Model Dev. 11, 1725–1752. https://gmd. copernicus.org/articles/11/1725/2018/.